# IRE1α RNase–dependent lipid homeostasis promotes survival in Myc-transformed cancers

Hong Xie,[1,2] Chih-Hang Anthony Tang,[3] Jun H. Song,[1,4] Anthony Mancuso,[1] Juan R. Del Valle,[5] Jin Cao,[6,7,8] Yan Xiang,[1] Chi V. Dang,[1] Roy Lan,[1] Danielle J. Sanchez,[1,4] Brian Keith,[1,2] Chih-Chi Andrew Hu,[3] and M. Celeste Simon[1,4]

[1]Abramson Family Cancer Research Institute and [2]Department of Cancer Biology, Perelman School of Medicine at the University of Pennsylvania, Philadelphia, Pennsylvania, USA. [3]The Wistar Institute, Philadelphia, Pennsylvania, USA. [4]Department of Cell and Developmental Biology, Perelman School of Medicine at the University of Pennsylvania, Philadelphia, Pennsylvania, USA. [5]Department of Chemistry, University of South Florida, Tampa, Florida, USA. [6]Department of Molecular and Cellular Biology, [7]Lester and Sue Smith Breast Center, and [8]Dan L. Duncan Cancer Center, Baylor College of Medicine, Houston, Texas, USA.

**Myc activation is a primary oncogenic event in many human cancers; however, these transcription factors are difficult to inhibit pharmacologically, suggesting that Myc-dependent downstream effectors may be more tractable therapeutic targets. Here, we show that Myc overexpression induces endoplasmic reticulum (ER) stress and engages the inositol-requiring enzyme 1α (IRE1α)/X-box binding protein 1 (XBP1) pathway through multiple molecular mechanisms in a variety of c-Myc– and N-Myc–dependent cancers. In particular, Myc-overexpressing cells require IRE1α/XBP1 signaling for sustained growth and survival in vitro and in vivo, dependent on elevated stearoyl-CoA-desaturase 1 (SCD1) activity. Pharmacological and genetic XBP1 inhibition induces Myc-dependent apoptosis, which is alleviated by exogenous unsaturated fatty acids. Of note, SCD1 inhibition phenocopies IRE1α RNase activity suppression in vivo. Furthermore, IRE1α inhibition enhances the cytotoxic effects of standard chemotherapy drugs used to treat c-Myc–overexpressing Burkitt's lymphoma, suggesting that inhibiting the IRE1α/XBP1 pathway is a useful general strategy for treatment of Myc-driven cancers.**

## Introduction

The Myc family of proto-oncogenes (*MYC*, *MYCN*, *MYCL*) encodes bHLHZ (basic helix-loop-helix leucine zipper) transcription factors, which regulate thousands of genes coordinating numerous cellular processes, including proliferation, differentiation, self-renewal, and metabolism (1). While Myc proteins exhibit variable expression patterns, they share considerable functional redundancy (2). Although *MYC* genes are normally induced by mitogenic stimulation and their activity is tightly regulated under physiological conditions, oncogenic activation occurring via mutation, genomic amplification, and translocation leads to aberrant overexpression or stabilization of Myc proteins (1).

Dysregulation of Myc oncoproteins is a frequent event in a broad array of human cancers, including Burkitt's lymphoma (BL), breast cancer, neuroblastoma (NB), etc. (1). The role of Myc in tumor initiation and maintenance makes it an appealing target for cancer therapy (3), although targeting transcription factors has generally proven difficult. Despite an increasingly detailed mechanistic understanding of Myc structure and function, therapeutic strategies to directly manipulate Myc remain a historic challenge (4–7), suggesting that alternative approaches are needed.

One important consequence of Myc activation is enhanced ribosome biogenesis and protein synthesis, required for its oncogenic output and cancer cell survival (8). Oncogenic Myc can thus engage the unfolded protein response (UPR), a cellular homeostatic program initiated by an excess of unfolded or misfolded proteins in the endoplasmic reticulum (ER) lumen (9). In mammalian cells, the UPR has evolved into a complex network of signaling events, mediated by 3 major stress sensors: inositol-requiring enzyme 1 (IRE1), activating transcription factor 6 (ATF6), and PKR-like endoplasmic reticulum kinase (PERK). Each sensor engages unique mechanisms to affect distinct transcription factors, initiating a specific molecular response. Interestingly, PERK promotes an autophagic program that sustains cell viability and promotes tumor growth in c-Myc–overexpressing cells (10, 11). In contrast, a role for the IRE1 pathway in Myc-overexpressing cells and its potential utility as a therapeutic target for Myc-driven cancers have not been investigated.

IRE1 is the only ER stress sensor conserved from yeast to mammals, and the mammalian genome encodes 2 isoforms, IRE1α and IRE1β. IRE1α is more ubiquitously expressed, whereas IRE1β is restricted to the epithelium of the gastrointestinal tract (12). IRE1 proteins have an ER-luminal sensor domain that recognizes unfolded proteins as well as cytosolic kinase and endoribonuclease (RNase) domains that mediate responses through downstream effectors (12) (see Figure 1A). Under conditions of ER stress, IRE1 is activated through dimerization and autophosphorylation and removes 26 nucleotides from unspliced X-box binding protein 1 (*XBP1u*) mRNA to generate spliced *XBP1* (*XBP1s*), producing a functional XBP1s transcription factor (Figure 1A) (12). XBP1s in turn regulates the expression of numerous genes that maintain ER homeostasis, including those encoding ER-resident chaperones and components of the ER-associated degradation machinery (ERAD) (13, 14). The IRE1 RNase also selectively degrades ER-bound mRNAs to alleviate ER protein load, a process known as regulated IRE1-dependent decay (RIDD) (15).

**Conflict of interest:** The authors have declared that no conflict of interest exists.
**Submitted:** June 28, 2017; **Accepted:** January 16, 2018.
**Reference information:** *J Clin Invest.* 2018;128(4):1300–1316.
https://doi.org/10.1172/JCI95864.

In this study, we demonstrate that the IRE1α/XBP1 pathway is engaged in both c-Myc– and N-Myc–driven cancers and that c-Myc regulates this pathway through multiple molecular mechanisms. Moreover, IRE1α/XBP1 signaling induces stearoyl-CoA desaturase (*SCD*) transcription, which generates unsaturated lipids required for ER membrane homeostasis. Pharmacological inhibition of IRE1α RNase activity or XBP1 depletion decreases growth and initiates apoptosis preferentially in Myc-overexpressing cells in vitro and in vivo and is reversed by exogenous unsaturated lipids. Treatment with a SCD inhibitor phenocopies the effects of IRE1α suppression on in vivo tumor growth. Finally, a highly selective IRE1α inhibitor (B-I09) exhibits synergistic effects with standard of care (e.g., doxorubicin) to treat c-Myc–transformed BL. Taken together, these findings reveal an essential mechanism whereby oncogene-driven anabolic metabolism engages homeostatic stress responses to promote tumor growth. Importantly, the use of IRE1α inhibitors (such B-I09) could improve treatment of both c-Myc–driven (e.g., BL) and N-Myc–driven (e.g., NB) malignancies.

## Results

*ER stress and the IRE1α/XBP1 pathway are enhanced in human and mouse BL*. Previous reports suggested a relationship between c-Myc expression and ER stress, although the details of this interaction remain unclear (10). We employed BL as a c-Myc–dependent disease model in which *MYC* translocation into immunoglobulin loci leads to its constitutive transcriptional dysregulation and expression (16). Analysis of Oncomine data (www.oncomine.org) revealed that *HSPA5* mRNA, which encodes the ER chaperone BiP, is elevated in BL cells relative to normal centroblasts (CB) (Figure 1B), BL cells of origin. *HSPA5* levels also correlated with *MYC* mRNA abundance and an established c-Myc signature (Figure 1C, Supplemental Figure 1A, and Supplemental Table 1; see Methods for details; supplemental material available online with this article; https://doi.org/10.1172/JCI95864DS1), suggesting that increased c-Myc engages ER stress–response pathways in BL patients. We initially focused on the IRE1α arm of the UPR, whose regulatory and functional mechanisms have not been previously investigated in this setting. Gene-expression profiles of 2 independent BL patient cohorts (17, 18) revealed that elevated XBP1s target mRNAs (19) relative to CB (Figure 1D), consistent with increased IRE1α RNase activity and XBP1s accumulation. Interestingly, RIDD was not engaged, as indicated by the overexpression (rather than underexpression) of multiple RIDD targets in BL (Supplemental Figure 1B). In addition, ratios of *Xbp1s* to total *Xbp1* (*Xbp1t*) transcripts, an indicator of IRE1α RNase activity, were elevated in *Eλ/MYC* murine BL lymphoma cells and *LAP/MYC* murine hepatocellular carcinoma cells compared with their normal counterparts (Figure 1E and Supplemental Figure 1C), demonstrating that elevated c-Myc induces IRE1α RNase activity in multiple cancer types.

*c-Myc activation initiates ER stress and the IRE1α/XBP1 pathway through multiple mechanisms*. To study the effect of c-Myc on ER stress responses, we employed human P493 B cell lymphoma cells, in which c-Myc levels can be manipulated with tetracycline and β-estradiol (20) (annotated as No Myc, Low Myc, and High Myc) (Supplemental Figure 2A). Cell proliferation, cell size, and protein content increased proportionally with c-Myc abundance (Figure 2, A and B, and Supplemental Figure 2, A and B), as did total RNA content (Supplemental Figure 2C). Along with the canonical target gene *LDHA* (Supplemental Figure 2D), c-Myc induction correlated with elevated *ERN1* (IRE1α), *HSPA5* (BiP), *XBP1t*, *XBP1s* (XBP1s), and *XBP1s/XBP1t* (Figure 2, C–E), suggesting that c-Myc regulates multiple components of the IRE1α stress-response pathway in these cells.

c-Myc appeared to induce the IRE1α/XBP1 pathway through a variety of mechanisms. First, restimulation of previously c-Myc–depleted P493 cells via tetracycline withdrawal revealed a time-dependent increase in *LDHA*, *ERN1*, *HSPA5*, *XBP1t*, and *XBP1s* mRNA (Figure 2F and Supplemental Figure 2E) and protein (Figure 2G), with maximal expression levels achieved by 24 to 48 hours. Importantly, IRE1α, BiP, XBP1s, and c-Myc protein levels in P493 High Myc cells were comparable to multiple bona fide BL cell lines: Raji, Daudi, Ramos, and EB-2 (Supplemental Figure 2F), consistent with the notion that P493 High Myc cells are a faithful BL model (20). ChIP-sequencing (ChIP-seq) analysis of P493 cells confirmed c-Myc binding to E-box sequences in the *ERN1*, *HSPA5*, and *XBP1* promoters, confirming that c-Myc activates their transcription directly (Supplemental Figure 2G). Second, c-Myc regulates IRE1α RNase activity, as demonstrated by increased *XBP1s/XBP1u* ratios (Figure 2D) and phosphorylated IRE1α protein levels (Figure 2E) in c-Myc–expressing cells. Consistent with this observation, *XBP1s/XBP1t* ratios were reduced upon c-Myc suppression, but only fully restored 48 hours after c-Myc induction (Figure 2, F and G). These data likely reflect a delay between c-Myc–dependent target gene induction (<24 hours) and accumulation of sufficient misfolded/unfolded proteins to stimulate IRE1α RNase activity (between 24 hours and 48 hours). Third, utilizing a cycloheximide (CHX) chase assay, we observed that IRE1α protein half-life was regulated by c-Myc (Supplemental Figure 2H). IRE1α protein stability can be positively regulated by DDRGK domain–containing protein 1 (DDRGK1) through ufmylation modification (21). However, in contrast to a previous study, this may be DDRGK1 independent in BL, as DDRGK1 expression was negatively correlated with IRE1α stability in P493 cells (Supplemental Figure 2I). In addition, Sun et al. demonstrated that IRE1α is a substrate of the SEL1L-HRD1 ERAD complex and that ERAD-mediated IRE1α degradation is attenuated by ER stress (22). However, no significant changes in SEL1L1 or HRD1 protein levels were observed in P493 cells with variable c-Myc expression (Supplemental Figure 2, J and K), suggesting that the exact mechanism of how c-Myc regulates IRE1α protein stability needs to be further investigated.

Treating c-Myc–overexpressing BL cell lines with the nonspecific Myc inhibitor JQ1 (Supplemental Figure 2, L and M) or low-dose CHX (Supplemental Figure 2N) significantly reduced *HSPA5* and *XBP1s* transcripts and proteins as well as *XBP1s/XBP1t* ratios. Consistent with these biochemical findings, transmission electron microscopy revealed an irregular ER structure, with substantially expanded membranes and distended lumens in c-Myc–overexpressing P493 cells (Figure 2H). Taken together, our data are consistent with a model in which c-Myc engages the IRE1α/XBP1 stress pathway through multiple mechanisms (Figure 2I) by (a) directly activating *ERN1*, *HSPA5,* and *XBP1* transcription, (b) stabilizing IRE1α protein, and (c) increasing ER protein load, thereby activating IRE1α RNase activity and promoting *XBP1* splicing (See Discussion).

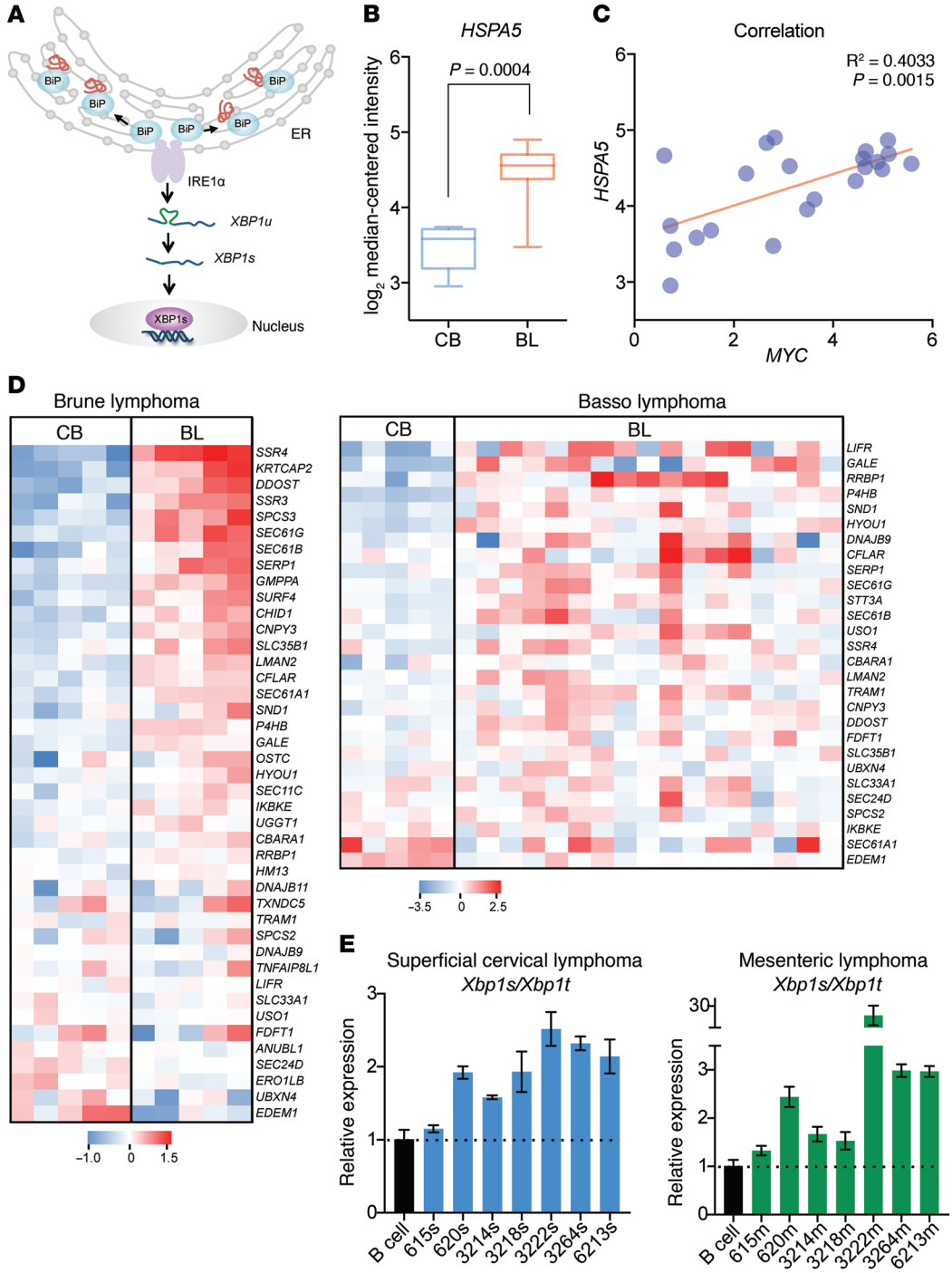


**Figure 1. ER stress and IRE1α/XBP1 signaling are enhanced in human and mouse BL.** (**A**) Schematic model of the IRE1α/XBP1 pathway. (**B**) $\log_2$ median-centered intensity of *HSPA5* in human BL ($n$ = 17) and CB ($n$ = 5, 2-tailed Student's $t$ test). Microarray data were obtained from the Oncomine database. Whiskers denote the minimal to maximal values. (**C**) Correlation of *MYC* and *HSPA5* in samples from **B**. $R^2$ and $P$ values were determined by a 2-tailed Pearson correlation test. (**D**) In 2 independent cohorts of BL patients and CB controls, heatmap shows the relative expression of genes directly regulated by XBP1s. Data were extracted from the Oncomine database. Expression signals are depicted using pseudocoloring, in which expression for each gene is shown as high (red) or low (blue). (**E**) qRT-PCR analysis of *Xbp1s/Xbp1t* ratios in mixed B lymphocytes isolated from 2 WT mouse spleens and tumor cells from superficial and mesenteric lymphomas in 7 *Eλ/MYC* mice. *Actb* was utilized as the endogenous control gene, and relative mRNA expression was determined by normalizing to expression in WT B lymphocytes. Three technical triplicates were used in each sample.

*Synthetic lethality between c-Myc overexpression and IRE1α RNase activity inhibition in vitro and in vivo*. To investigate the effects of IRE1α inhibition in the context of c-Myc overexpression, we used the highly specific IRE1α RNase inhibitor B-I09 (Supplemental Figure 3A), which was previously shown to mimic XBP1 deficiency and suppress chronic lymphocytic leukemia (CLL) progression (23). B-I09 treatment resulted in a dose-dependent decrease in XBP1s protein in P493 High Myc cells

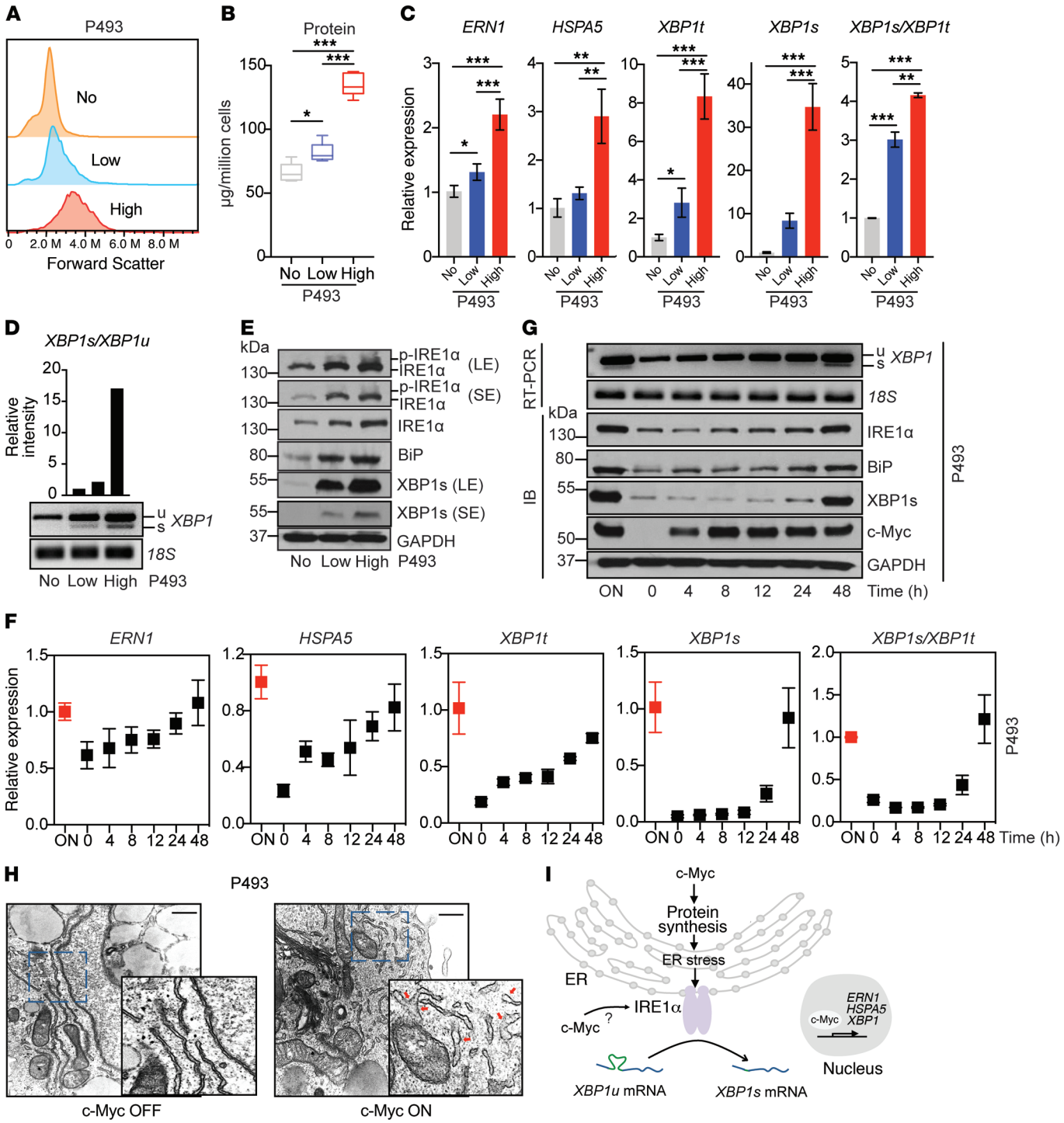


**Figure 2. c-Myc affects ER stress and the IRE1α/XBP1 pathway through multiple molecular mechanisms.** (**A**) P493 No Myc, Low Myc, and High Myc cells analyzed by flow cytometry to determine cell size using forward scatter (results are representative of >3 independent experiments). (**B**) Protein content of 1 million P493 No Myc, Low Myc, and High Myc cells ($n$ = 6, 2-way ANOVA test with Bonferroni's correction). (**C**) qRT-PCR analysis of *ERN1*, *HSPA5*, *XBP1t*, *XBP1s*, and *XBP1s/XBP1t* ratios in P493 cells with different levels of c-Myc ($n$ = 3, 2-way ANOVA test with Bonferroni's correction). (**D**) RT-PCR analysis of *XBP1* splicing in P493 cells. (**E**) Immunoblot analysis for IRE1α phosphorylation (phos-tag SDS-PAGE), BiP, and XBP1s in P493 cells. SE, short time exposure; LE, long time exposure. (**F**) In P493 cells, c-Myc was suppressed with tetracycline (0.1 µg/ml) for 24 hours, which was then withdrawn to reexpress c-Myc. At indicated times, mRNA was collected for qRT-PCR analysis. Three technical triplicates were used in each sample, and results are representative of more than 3 independent experiments. (**G**) Corresponding RT-PCR and immunoblot analysis of data in **F**. (**H**) Comparison of ER structures using transmission electron microscopy in P493 cells with or without c-Myc overexpression. Scale bars: 500 nm. (**I**) Schematic model of c-Myc regulating ER stress and the IRE1α/XBP1 pathway. For qRT-PCR, *ACTB* was utilized as the endogenous control gene. $^*P < 0.05$; $^{**}P < 0.01$; $^{***}P < 0.001$.

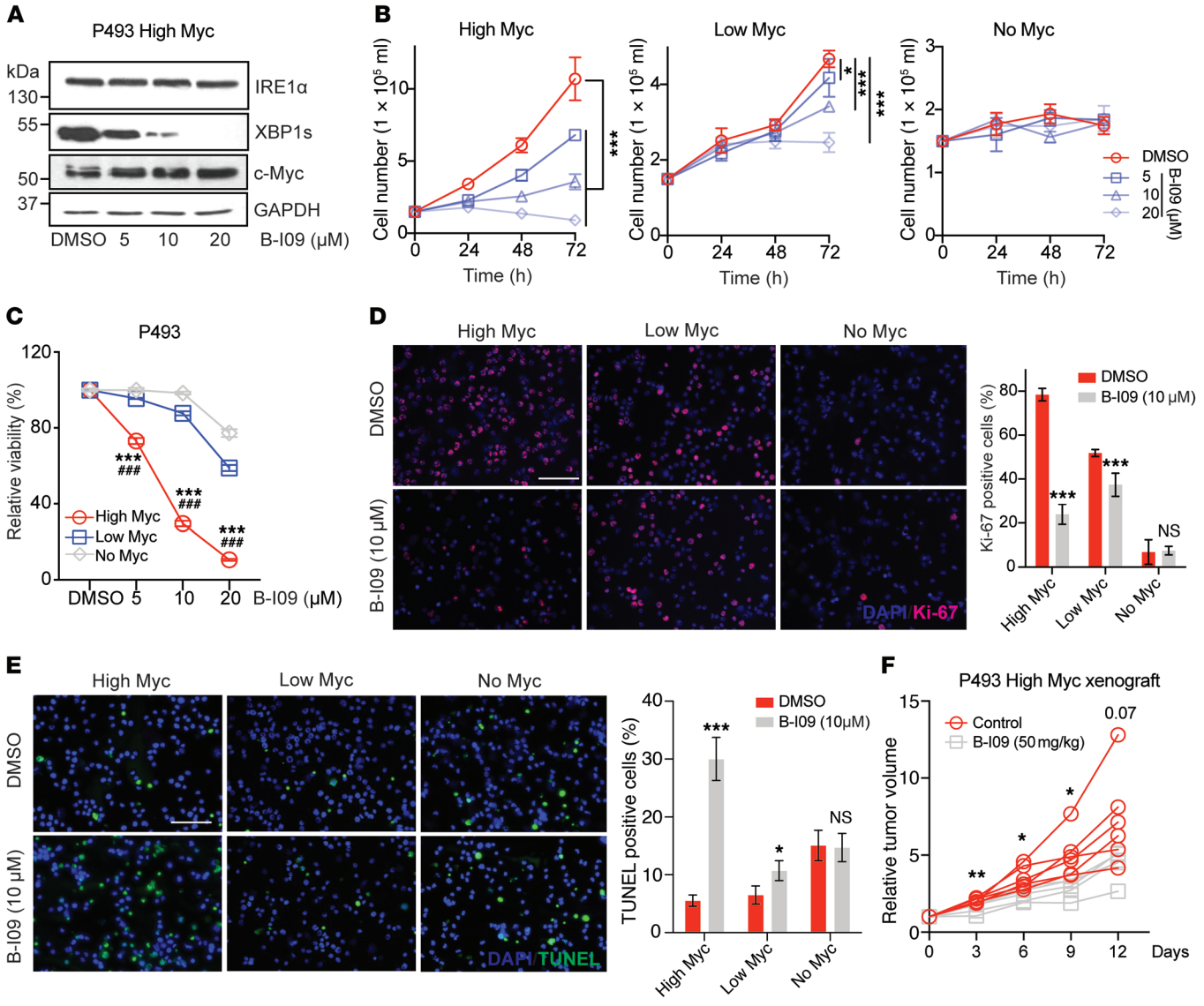


**Figure 3. Synthetic lethality between c-Myc overexpression and IRE1α RNase inhibition in vitro and in vivo.** (**A**) P493 High Myc cells treated with indicated concentrations of B-I09 for 24 hours; 5 μg/ml tunicamycin was added 6 hours before harvest. Immunoblots show the expression of IRE1α, XBP1s, and c-Myc. (**B**) Cells cultured with B-I09 and counted at indicated times ($n$ = 3). (**C**) Cells treated with indicated concentrations of B-I09 for 48 hours. Viability was determined by FITC–annexin V/propidium iodide (PI) staining (as for all viability assays). Relative viability was determined by normalizing to viability of cells with DMSO treatment. (**D** and **E**) Ki67 and TUNEL staining representative images (left) and quantifications (right) upon 10 μM B-I09 treatment for 48 hours. Five fields per slide were quantified. Scale bars: 100 μm. (**F**) Growth of P493 High Myc subcutaneous tumors treated with vehicle or B-I09 (50 mg/kg intraperitoneally, once per day, 5 days per week, 2 weeks). Relative tumor volume was determined by normalizing to volume when treatment was started ($n$ = 6 for control, $n$ = 5 for B-I09, 2-tailed Student's $t$ test). For cell viability assays, data are representative of 3 independent experiments. Two-way ANOVA with Bonferroni's correction was used to determine significance, if not specified elsewhere. $^{*}P < 0.05$, $^{**}P < 0.01$, $^{***}P < 0.001$ (**B** and **D**–**F**); $^{***}P < 0.001$, High Myc vs. Low Myc, $^{\#\#\#}P < 0.001$, High Myc vs. No Myc (**C**).

treated with tunicamycin (Figure 3A), which blocks N-linked glycosylation and amplifies ER stress (24) without altering c-Myc levels (Figure 3A) or IRE1α phosphorylation (Supplemental Figure 3B). Similarly, B-I09–treated P493 High Myc cells displayed a dose-dependent decrease in cell proliferation and viability (Figure 3, B and C, and Supplemental Figure 3C). Importantly, the effects of B-I09 were more subtle in Low Myc and No Myc cells, especially at 10 μM or less (Figure 3, B–E and Supplemental Figure 3D). It is noteworthy that the ability of B-I09 to specifically induce apoptosis in c-Myc–overexpressing cells was significantly higher than that of doxorubicin, a traditional chemotherapeutic drug targeting highly proliferating cells, or that of JQ1 (Supplemental Figure 3E). We also evaluated 3 CLL cell lines (MEC1, MEC2, and WaC3) with variable c-Myc levels (Supplemental Figure 3F). Although WaC3 cells grow more slowly than MEC1 and MEC2 CLL cells (Supplemental Figure 3F), they were more sensitive to B-I09 treatment–induced growth arrest and apoptosis (Supplemental Figure 3G). These results decrease the possibility that variable cell proliferation rates between P493 High Myc, Low Myc, and No Myc cells are a confounding factor

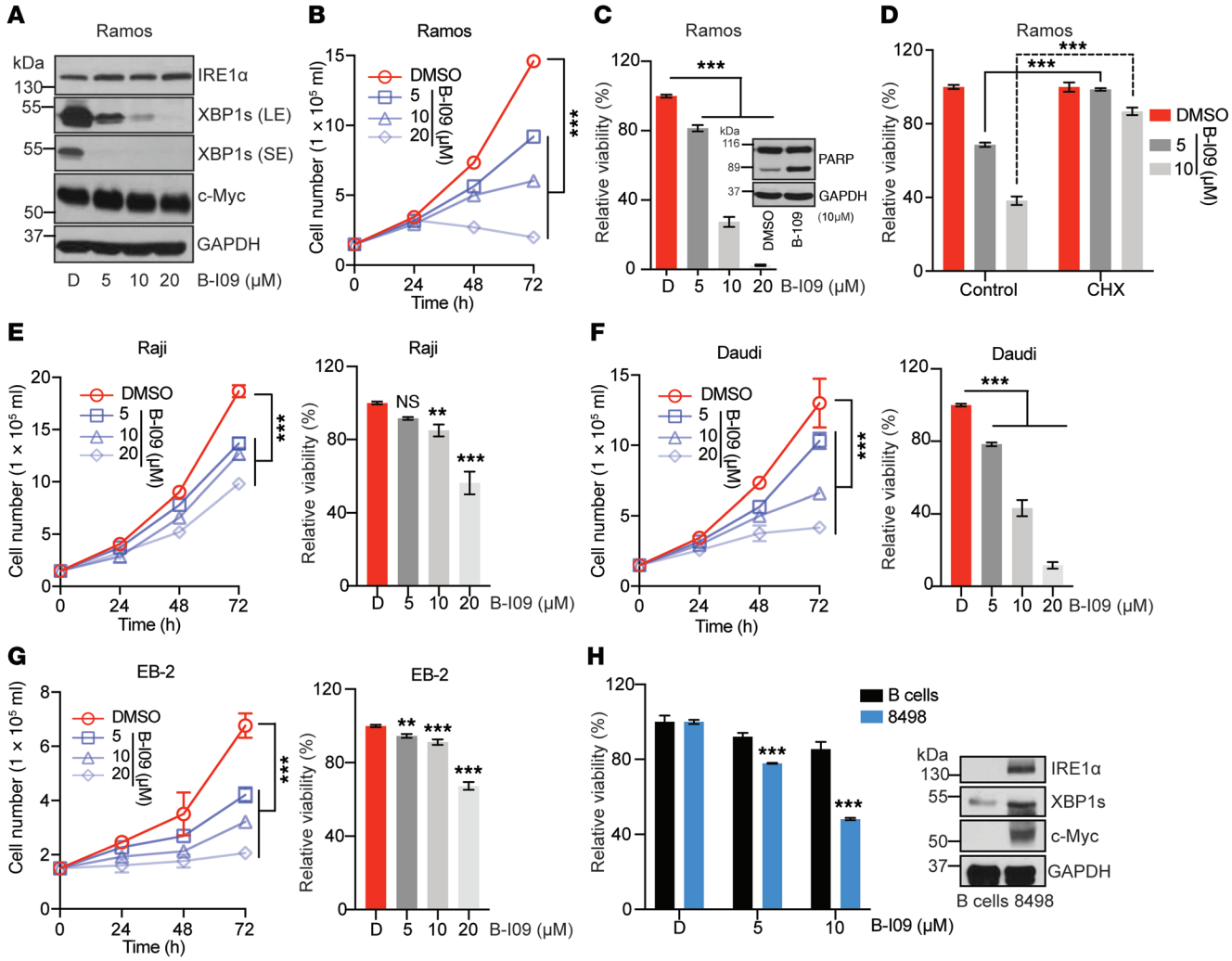


**Figure 4. B-I09 suppresses growth and induces apoptosis in human and mouse BL cells.** (**A**–**C**) Ramos cells were treated with indicated concentrations of B-I09 for 24 hours (**A**), 48 hours (**C**), or 72 hours (**B**). Western blot shows the expressions of IRE1α, XBP1s, and c-Myc (**A**). Cell numbers were counted at indicated times (**B**) ($n$ = 3). Cell viability was examined and relative cell viability was determined by normalizing to viability upon DMSO treatment (**C**). (**D**) Ramos cells pretreated with CHX (0.5 μg/ml) for 2 hours and then cultured with DMSO, 5 μM, or 10 μM B-I09 for 48 hours. Cell viability was then examined and relative cell viability determined by normalizing to viability upon DMSO treatment or DMSO+CHX treatment, respectively. (**E**–**G**) Raji, Daudi, and EB-2 BL cells treated with B-I09 for the indicated times. Cell numbers were counted ($n$ = 3) and cell viability examined. (**H**) For B cells isolated from WT mouse spleens and 8498 cells from *Eκ/MYC* lymphoma tumor, protein expression of IRE1α, XBP1s, and c-Myc was compared and their sensitivities to different B-I09 concentrations at 48 hours examined. For all viability assays, results are representative of 3 independent experiments. $P$ values were determined by 2-way ANOVA with Bonferroni's correction. $^{**}P < 0.01$; $^{***}P < 0.001$.

and confirm that c-Myc overexpression could be an important indicator for B-I09 usage in different types of cancers. Similar effects were observed using 4μ8c, a distinct (albeit less potent) IRE1α RNase inhibitor (23, 25) (Supplemental Figure 3, H and I). Finally, B-I09 treatment inhibited P493 High Myc xenograft tumor growth in vivo (Figure 3F), with no obvious toxicity, as indicated by the maintenance of mouse body weight during treatment (Supplemental Figure 3J).

*B-I09 suppresses growth and induces apoptosis in human and mouse BL cells*. c-Myc was overexpressed in all BL cells tested (Supplemental Figure 2F), which also exhibited growth and survival defects upon B-I09 exposure, although their sensitivity to the drug varied (Figure 4, A–G). For example, B-I09–treated Ramos cells displayed a dose-dependent inhibition of *XBP1* splicing and reduced proliferation and viability without apparent alterations in c-Myc protein levels or IRE1α phosphorylation (Figure 4, A–C, and Supplemental Figure 4A). The modest increase in IRE1α protein abundance (Figure 4A) was consistent with that found in previous studies of XBP1 deletion in leukemic and hepatic cells and may reflect a negative feedback mechanism (23, 26) or changes in IRE1α protein stability. Importantly, the viability of B-I09–treated Ramos cells was rescued by treatment with CHX (Figure 4D), indicating that elevated protein synthesis and proteotoxicity at least partially contribute to IRE1α activation. We employed Ramos (EBV$^-$) and Daudi (EBV$^+$) cells as representative of 2 categories of human BL (EBV$^-$ and EBV$^+$) (27) for further study (see below). Finally, elevated IRE1α and XBP1s expression and increased sensitivity to B-I09 were observed in 8498 cells isolated from the *Eκ/MYC* mouse lymphoma model as

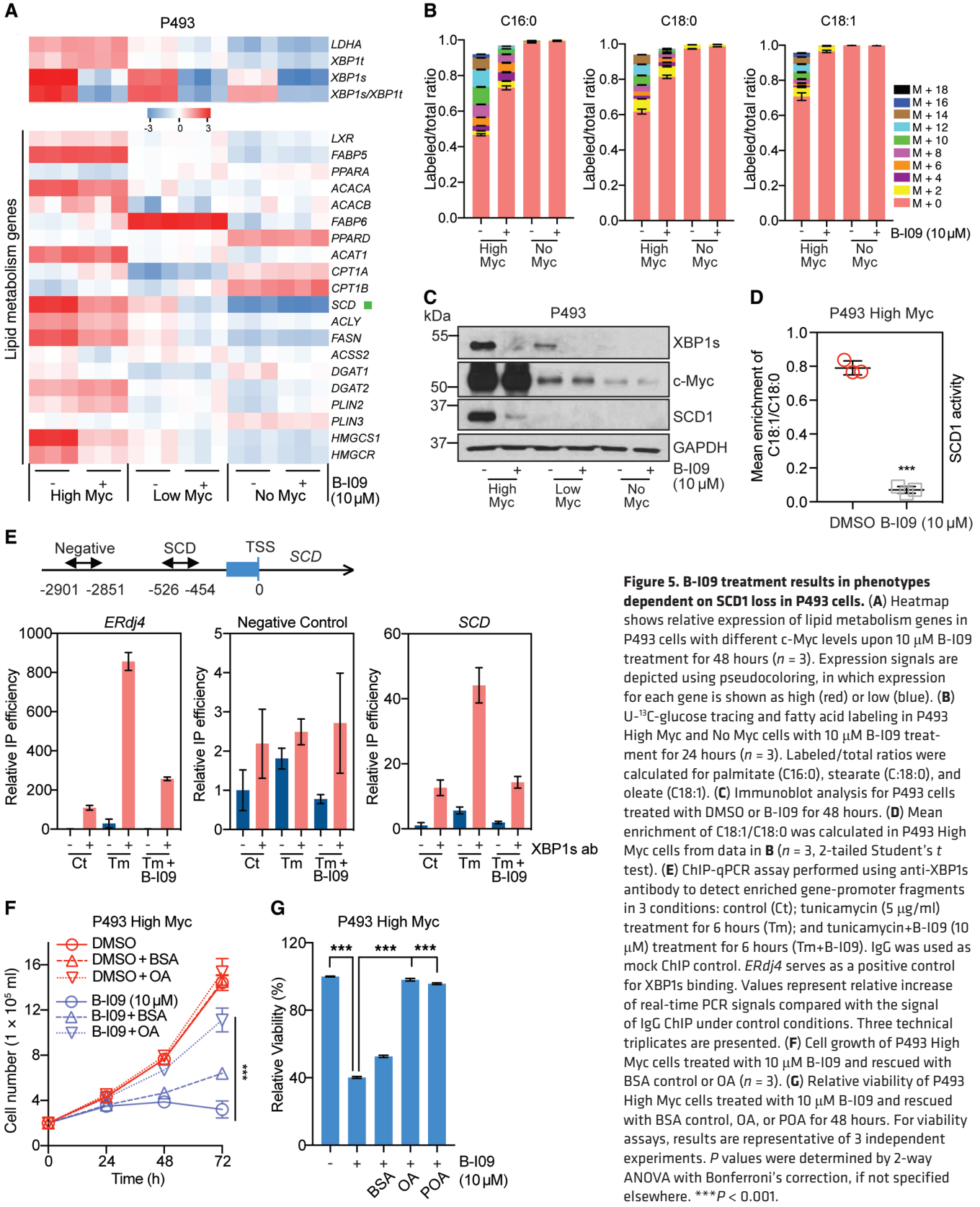


**Figure 5. B-I09 treatment results in phenotypes dependent on SCD1 loss in P493 cells.** (**A**) Heatmap shows relative expression of lipid metabolism genes in P493 cells with different c-Myc levels upon 10 μM B-I09 treatment for 48 hours ($n$ = 3). Expression signals are depicted using pseudocoloring, in which expression for each gene is shown as high (red) or low (blue). (**B**) U-$^{13}$C-glucose tracing and fatty acid labeling in P493 High Myc and No Myc cells with 10 μM B-I09 treatment for 24 hours ($n$ = 3). Labeled/total ratios were calculated for palmitate (C16:0), stearate (C:18:0), and oleate (C18:1). (**C**) Immunoblot analysis for P493 cells treated with DMSO or B-I09 for 48 hours. (**D**) Mean enrichment of C18:1/C18:0 was calculated in P493 High Myc cells from data in **B** ($n$ = 3, 2-tailed Student's $t$ test). (**E**) ChIP-qPCR assay performed using anti-XBP1s antibody to detect enriched gene-promoter fragments in 3 conditions: control (Ct); tunicamycin (5 μg/ml) treatment for 6 hours (Tm); and tunicamycin+B-I09 (10 μM) treatment for 6 hours (Tm+B-I09). IgG was used as mock ChIP control. *ERdj4* serves as a positive control for XBP1s binding. Values represent relative increase of real-time PCR signals compared with the signal of IgG ChIP under control conditions. Three technical triplicates are presented. (**F**) Cell growth of P493 High Myc cells treated with 10 μM B-I09 and rescued with BSA control or OA ($n$ = 3). (**G**) Relative viability of P493 High Myc cells treated with 10 μM B-I09 and rescued with BSA control, OA, or POA for 48 hours. For viability assays, results are representative of 3 independent experiments. $P$ values were determined by 2-way ANOVA with Bonferroni's correction, if not specified elsewhere. ***$P < 0.001$.

compared with WT murine B lymphocytes (Figure 4H). Collectively, these data suggest an essential protective role for IRE1α RNase activity downstream of elevated c-Myc in BL cells.

*IRE1α RNase inhibition induces growth and viability defects by decreasing SCD1 accumulation.* There are multiple mechanisms whereby IRE1α might regulate growth and survival in c-Myc–overexpressing cells. For example, the IRE1α cytoplasmic region also contains a kinase domain that phosphorylates and activates the JNK pathway, inducing apoptosis (28). However, phospho-JNK protein levels were unaffected by B-I09 treatment (Supplemental Figure 5A). Additionally, XBP1s can regulate the expression of *BECN1*, thereby inducing autophagy (29, 30), which confers a cytoprotective advantage in c-Myc–overexpressing mammalian (10) and *Drosophila* (11) cells. However, autophagy (based on p62 and LC3-II abundance) was not suppressed by B-I09 treatment (Supplemental Figure 5B), indicating no decline in autophagic flux in this setting.

Both c-Myc and the IRE1α/XBP1 pathway have been previously implicated in regulating lipid metabolism in normal and malignant tissues (19, 26, 31–33), suggesting that alterations in lipid homeostasis trigger growth and viability defects in IRE1α-inhibited, c-Myc–overexpressing BL cells. To investigate this possibility, we quantified mRNA levels of 20 lipid metabolism genes in IRE1α inhibitor–treated P493 cells, including those involved in synthesis, storage, and catabolism (Figure 5A). B-I09 treatment inhibited *XBP1* splicing without altering c-Myc activity (based on unchanged *LDHA* levels). Expression of lipid synthesis genes, e.g., *HMGCR1*, *HMGCS1*, *ACLY*, *ACACA*, *FASN*, and *SCD*, was increased by c-Myc and inhibited by B-I09. De novo lipogenesis generated diverse free fatty acids from glucose and glutamine, which could be probed by supplying uniformly $^{13}$C-labeled glucose (U-$^{13}$C-glucose) and subsequent mass spectrometry (MS) analysis of saponified fatty acids (34) (Supplemental Figure 5C). Analysis of labeling at steady state quantified the unlabeled fraction (M+0) relative to labeled forms arising from lipogenesis. Consistent with mRNA expression, de novo lipogenesis was significantly higher in High Myc cells and suppressed by B-I09 treatment (Figure 5B).

We focused on *SCD* for several reasons: (a) *SCD* mRNA abundance was the most altered across different conditions among all genes tested (Figure 5A); (b) *SCD* encodes the rate-limiting enzyme in monounsaturated fatty acid formation (furthermore, increased levels of monounsaturated fatty acids [e.g., C18:1 oleic acid (OA)] are a hallmark of human c-Myc–driven lymphomas, based on comprehensive lipid profiling; ref. 35); and (c) previous work demonstrated that synthesizing or scavenging unsaturated lipids is critical to maintaining cell viability in multiple transformed cell types, especially encountering elevated protein synthesis (36, 37). Decreased SCD1 protein accumulation upon IRE1α RNase inhibition was confirmed in multiple cell lines (Figure 5C and Supplemental Figure 5, D and E). More importantly, U-$^{13}$C-glucose labeling enabled us to determine SCD1 activity by calculating mean enrichment of labeled C18:1/C18:0 (Supplemental Figure 5C): SCD1 enzymatic activity was dramatically inhibited by B-I09 effects on SCD1 abundance (Figure 5D).

ChIP analysis demonstrated XBP1s binding to the *SCD* proximal promoter, regulated by both tunicamycin (utilized to increase XBP1s expression) and B-I09 (Figure 5E), consistent with previous observations in mouse liver cells (26). XBP1 knockdown resulted in decreased levels of SCD1 protein (Supplemental Figure 5F). *SCD* is a known c-Myc transcriptional target (38) (Figure 5A); however, c-Myc protein levels were only modestly changed, if at all, in response to IRE1α RNase inhibition (Figure 5C, and Supplemental Figure 5, D and E), suggesting that decreased SCD1 was at least partly c-Myc independent and XBP1s dependent. In summary, we identified *SCD* as a transcriptional target downstream of IRE1α/XBP1 signaling in BL.

To test the critical role of SCD1 in IRE1α-inhibited, c-Myc–overexpressing conditions, P493 High Myc cells were cultured with the monounsaturated fatty acids oleic acid (OA) (C18:1) or palmitoleic acid (POA) (C16:1). OA partly rescued cell proliferation (Figure 5F), and both OA and POA essentially restored cell viability without affecting the ability of B-I09 to reduce XBP1s and SCD1 expression (Figure 5G, and Supplemental Figure 5G). However, a combination of OA and saturated palmitic acid (Palm) (C16:0) did not rescue viability as effectively as OA alone, even though exposure to Palm itself was not toxic (Supplemental Figure 5H). These results suggest that unsaturated fatty acids are critical to maintaining the viability of B-I09–treated cells.

Because long-chain fatty acids are relatively insoluble in aqueous solutions, they were conjugated to lipid-free BSA before use. Surprisingly, control BSA partially rescued cell growth and viability in the absence of exogenous OA (Figure 5, F and G; and Supplemental Figure 5H). This raised the possibility that BSA might enter B-I09–treated cells through macropinocytosis (39, 40) and contribute to viability by supplying free amino acids, although free BSA could rescue viability by scavenging lipids in the medium (41). To test this, cells were cultured in medium with reduced lipid concentration (see Methods). Treatment with B-I09 substantially reduced cell viability in lipid-limited conditions, and whereas exogenous BSA alone rescued the viability of multiple B-I09–treated cell lines in replete medium, it had no significant effect on the survival of lipid-limited cells. In contrast, addition of exogenous BSA–conjugated OA fully rescued viability in lipid-limited cells, suggesting that BSA functioned primarily as a fatty acid shuttle in these experiments (Supplemental Figure 5I).

A requirement for SCD1 function in c-Myc–overexpressing P493 cells was further validated using a commercially available SCD1 inhibitor (SCDi), which phenocopied B-I09 treatment by inducing growth arrest and cell death (Supplemental Figure 5, J and K). However, apoptosis was only induced after 72 hours of treatment (Supplemental Figure 5K), suggesting other mechanisms might also exist.

The regulation of SCD1 by IRE1α/XBP1 signaling and its role in maintaining cell growth and survival were further validated in bona fide BL cell lines (Figure 6, A–D, and Supplemental Figure 6, A–D). Importantly, *SCD* expression was increased in BL cells relative to CB (Figure 6E). Therefore, we evaluated the therapeutic potential of SCDi for BL growth in vivo. SCDi administration significantly decreased tumor growth and tumor weight (Figure 6F). However, this was also accompanied by a slight weight loss during treatment (Supplemental Figure 6E), as observed in a previous study (42). Finally, SCDi treatment engaged all 3 UPR pathways (ATF6: *HERPUD1*; IRE1: *XBP1s*, *DNAJB9*; PERK: *ATF3*, *DDIT3*), and each was reversed with OA supplementation (Supplemental Figure 6F). Taken together, IRE1α RNase inhibition resulted in BL

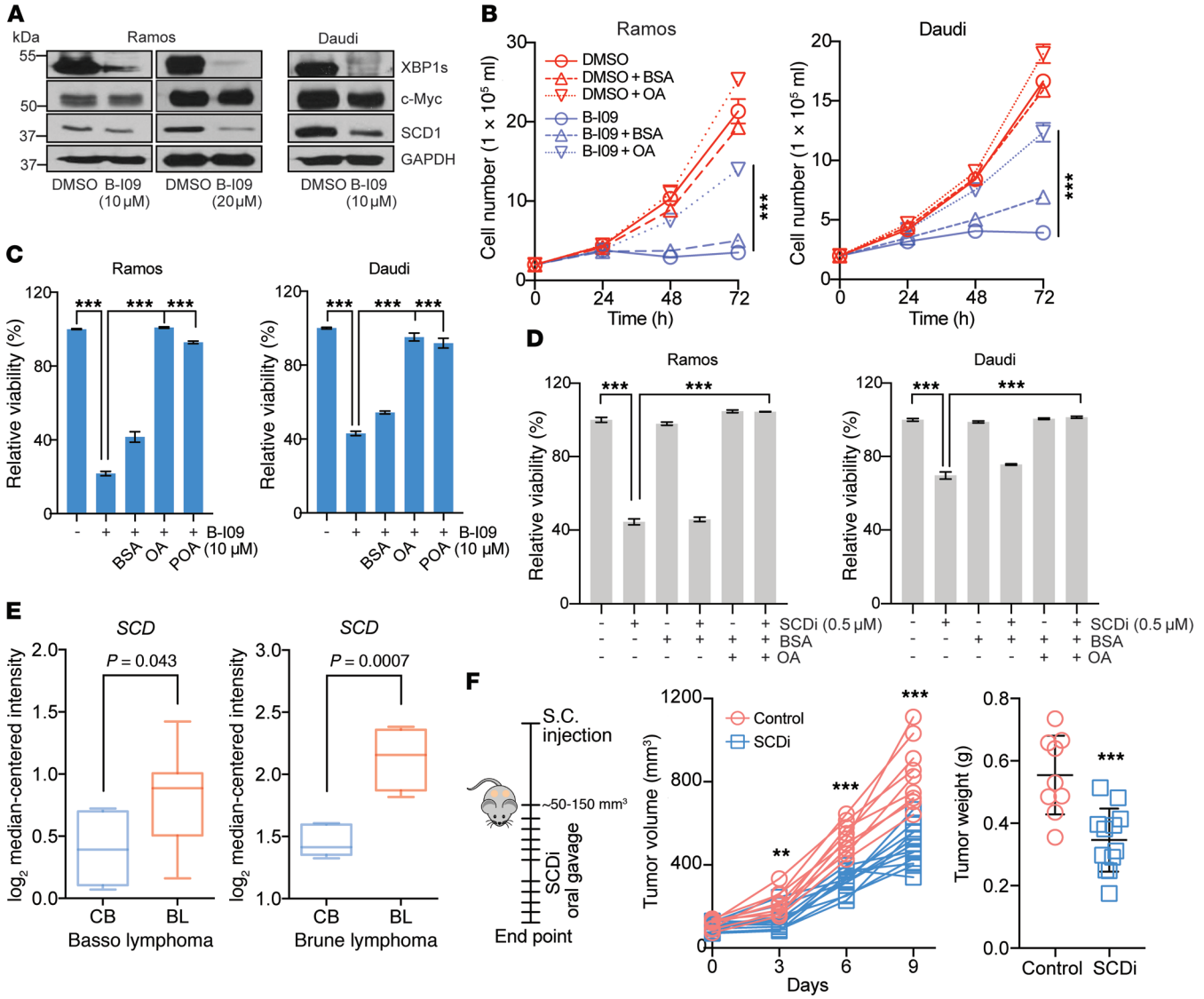


**Figure 6. B-I09 treatment results in phenotypes dependent on SCD1 loss in BL cells.** (**A**) Immunoblot analysis of Ramos and Daudi cells treated with indicated concentrations of B-I09 for 48 hours. (**B**) Cell growth ($n$ = 3) of Ramos and Daudi cells treated with B-I09 (20 μM for Ramos, 10 μM for Daudi) and rescued with BSA control or OA. (**C**) Relative viability of Ramos and Daudi cells treated with 10 μM B-I09 and rescued with BSA control, OA, or POA for 48 hours. (**D**) Relative viability of Ramos and Daudi cells treated with 0.5 μM SCDi and rescued with BSA control or OA for 48 hours. (**E**) Normalized reads of *SCD* in human BL and CB from healthy donors. Microarray data were obtained from the Oncomine database. Whiskers denote the minimal to maximal values. (**F**) Tumor growth and weight of xenografted Ramos tumors treated with control or SCDi (5 mg/kg, orally twice daily). For all viability assays, results are representative of 3 independent experiments. $^{**}P < 0.01$; $^{***}P < 0.001$, 2-way ANOVA with Bonferroni's correction (**B**–**D**); 2-tailed Student's $t$ test (**E** and **F**).

cell phenotypes, dependent on SCD1 loss. In addition, targeting SCD1 phenocopied B-I09 to decrease in vivo tumor growth. However, based on the toxicity of SCDi, IRE1α RNase inhibition may be a safer therapeutic strategy for BL patients.

*N-Myc–overexpressing cells also engage the IRE1α/XBP1/SCD1 pathway to maintain viability*. To determine whether these findings extend to other Myc family members, we employed the N-MycER SHEP NB cell line in which N-Myc activity is induced by tamoxifen treatment (Figure 7A; and Supplemental Figure 7A). N-Myc activation via 4-hydroxytamoxifen (4-OHT) increased *XBP1* splicing (Figure 7, B and C) and XBP1s protein abundance (Figure 7D), indicating that N-Myc also engages the IRE1α/XBP1 pathway. Whereas B-I09 had only modest effects on the proliferation of untreated control SHEP cells (N-Myc negative), it robustly inhibited proliferation and induced apoptosis in 4-OHT–treated N-Myc SHEP cells (N-Myc positive) in both dose- and time-dependent manners (Figure 7, E and F; and Supplemental Figure 7, B–D). Furthermore, this decrease in cell viability was largely restored by CHX treatment (Figure 7G). Mechanistically, B-I09 treatment resulted in decreased SCD1 (Figure 7H) and all phenotypes were partly or totally reversed by OA (Figure 7I and Supplemental Figure 7E). Similarly, N-Myc SHEP cells were more sensitive to SCDi treatment or *SCD* knockdown with siRNA than controls (Supplemental Figure 7, F–H). To confirm B-I09 IRE1α target specificity, cells were treated with scrambled shRNA (shSCR) or shRNA targeting *XBP1* (*shXBP1*) (Figure 8A). Like B-I09 treatment, XBP1 depletion with *shXBP1* decreased SCD1 protein levels and induced apoptosis in N-Myc SHEP cells, while control SHEP cells were largely resistant (Figure 8, A and B).

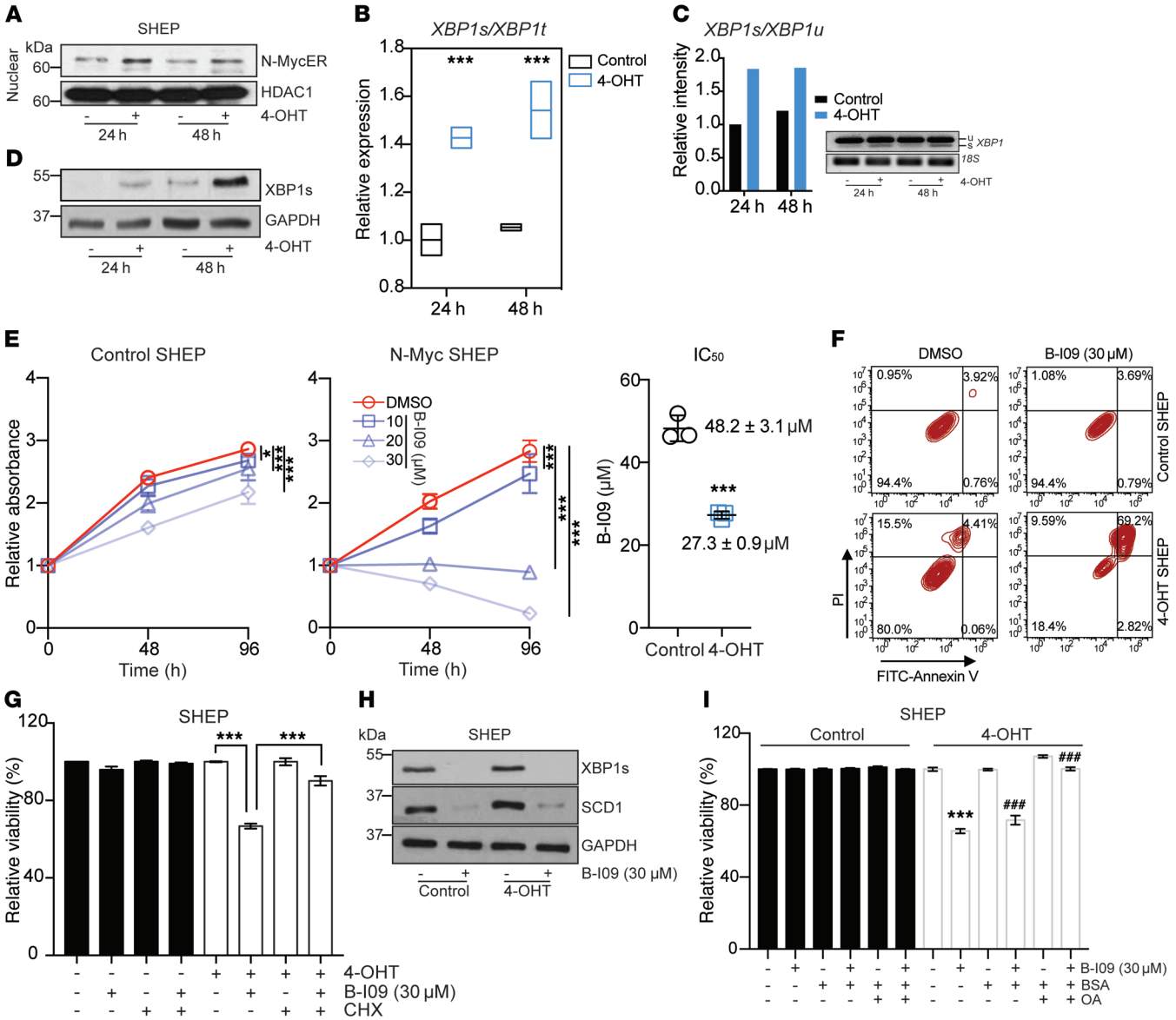


**Figure 7. N-Myc activates the IRE1α/XBP1 pathway, rendering cells vulnerable to XBP1s loss.** (**A**–**D**) SHEP N-MycER cells were treated with 4-OHT (200 nM) to activate N-Myc nuclear translocation (**A**). *XBP1s/XBP1t* ratios examined with qRT-PCR (**B**) ($n = 3$). *XBP1* splicing analyzed by RT-PCR (**C**) and XBP1s protein accumulation determined by immunoblots (**D**). (**E**) SHEP cells cultured in vehicle (control) or 4-OHT containing medium for 48 hours before treatment with DMSO or B-I09. WST-1 assay was used to examine cell growth. Relative absorbance was determined by normalizing to absorbance at time 0 hours ($n = 6$). $IC_{50}$ was then determined ($n = 3$, 2-tailed Student's *t* test). (**F**) Representative contour plots of control and 4-OHT SHEP cells treated with 30 μM B-I09 for 96 hours. (**G**) SHEP cells pretreated with CHX (0.5 μg/ml) for 2 hours and then cultured with DMSO or 30 μM B-I09 for 72 hours. Relative viability was determined by normalizing to viability upon DMSO treatment or DMSO+CHX treatment, respectively. (**H**) Immunoblot for control and 4-OHT SHEP cells with B-I09 treatment for 72 hours. (**I**) Control or N-Myc SHEP cells treated with DMSO or B-I09 and rescued with BSA or OA for 72 hours. Viability was examined and relative viability was determined by normalizing to viability upon DMSO treatment. For viability assays, results are representative of 3 independent experiments. *P* values were determined by 2-way ANOVA with Bonferroni's correction, if not specified elsewhere. $^{*}P < 0.05$, $^{***}P < 0.001$ (**B**, **E** and **B**, **E**, and **G**); $^{***}P < 0.001$, comparison of B-I09 and DMSO treatment; $^{###}P < 0.001$, comparison of B-I09+BSA or B-I09+OA and B-I09 treatment (**I**).

*MYCN* amplification is found in approximately 25% of NB cases and remains the best-characterized genetic marker of high-risk disease (43). We compared 3 NB cell lines with or without *MYCN* amplification: SK-N-AS (no *MYCN* amplification), BE2C (*MYCN* amplification), and Kelly (*MYCN* amplification). Cells with *MYCN* amplification expressed higher levels of *HSPA5* and *XBP1s* and exhibited enhanced sensitivity to B-I09 (Supplemental Figure 8, A and B). Importantly, XBP1 knockdown in Kelly cells dramatically impaired tumor growth in vivo (Figure 8C and Supplemental Figure 8, C and D). In summary, like c-Myc–overexpressing cells, N-Myc–overexpressing cells also engage the IRE1α/XBP1/SCD1 pathway to maintain viability, and targeting this axis could be a potential therapeutic strategy for N-Myc–overexpressing cancers, e.g., NB.

*B-I09 enhanced in vitro cytotoxicity of BL chemotherapeutic drugs.* Given the c-Myc–dependent toxicity of B-I09 observed in BL cell lines, we explored whether B-I09 treatment would

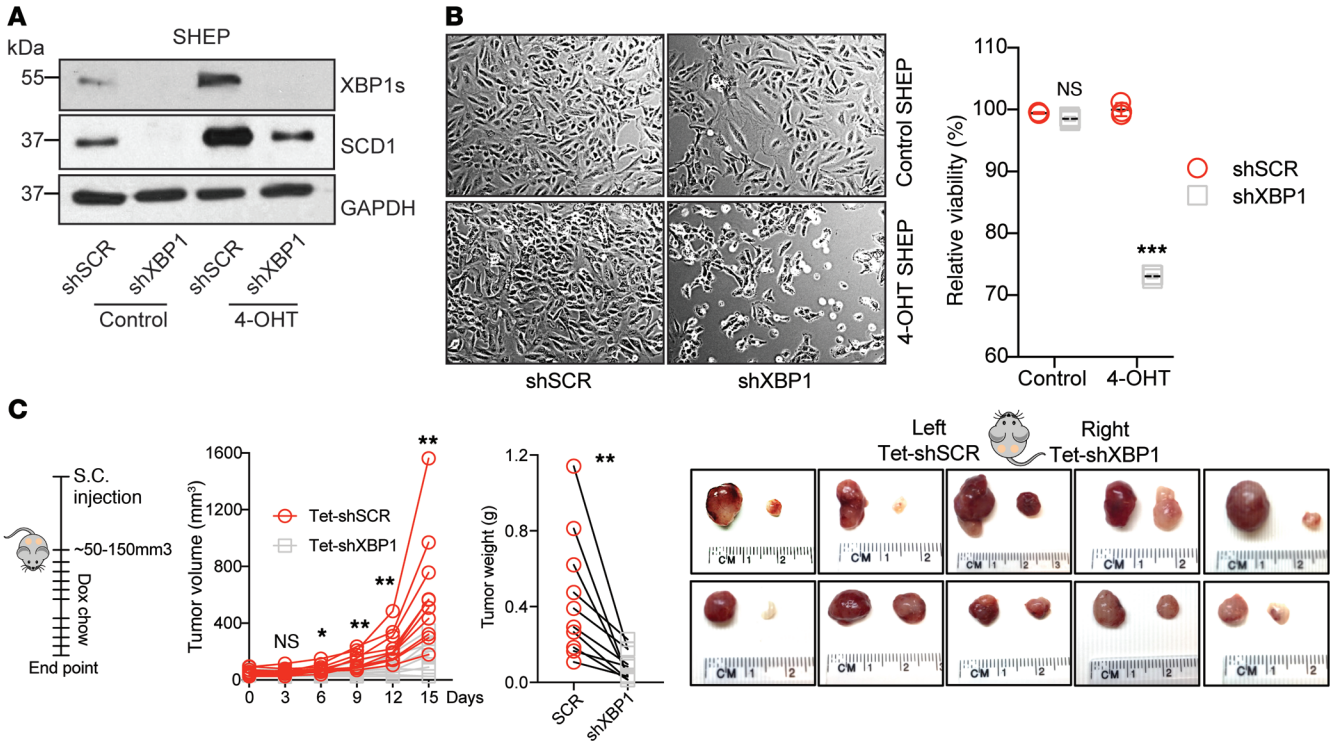


**Figure 8. XBP1 depletion results in apoptosis and tumor regression in N-Myc–overexpressing NB cells.** (**A** and **B**) SHEP cells infected with lentivirus containing shSCR or shXBP1 constructs for 48 hours and vehicle or 4-OHT subsequently added. After 72 hours, cells were imaged and harvested for immunoblot analysis and viability assays. For viability assays, results are representative of 3 independent experiments. *P* values were determined by 2-way ANOVA with Bonferroni's correction. (**C**) Kelly cells with tetracycline-inducible shSCR or shXBP1 constructs injected subcutaneously into the left or right flanks of mice, respectively. When tumor sizes reached 50–150 $mm^3$, doxycycline chow was used to knock down *XBP1*. Tumor growth, tumor weight, and bulk tumors are shown. $^*P < 0.05$; $^{**}P < 0.01$; $^{***}P < 0.001$, 2-tailed paired *t* test.

improve standard therapies currently used to treat BL clinically. Apoptosis triggered in BL cells by either doxorubicin or vincristine treatment was further enhanced by B-I09. Combination indices (CIs) showed additive or synergistic effects with doxorubicin and vincristine in Daudi and Ramos cells (Figure 9, A–C, and Table 1), and the effects of B-I09 depended on SCD1 activity (Supplemental Figure 9, A and B). These results suggest that B-I09 and other IRE1α inhibitors could be used to treat a variety of Myc-driven malignancies, including c-Myc–overexpressing BL and N-Myc–overexpressing NB, to improve standard of care.

## Discussion

Myc overexpression drives tumor growth and progression by altering the expression of thousands of target genes that regulate myriad cellular processes (1). Although Myc-transformed tumors are highly dependent on sustained Myc transcriptional activity, directly inhibiting Myc as a therapeutic approach has proven technically difficult and largely unsuccessful (7). Alternative approaches, such as inhibition of Myc-mediated downstream effectors, need to be investigated. Paradoxically, Myc is known to activate both proliferation and apoptosis, depending on the cellular context (1, 44). However, the mechanisms that cancer cells use to escape Myc-induced apoptosis remain poorly understood. In this study, we found Myc activated the prosurvival IRE1α/XBP1 pathway in a broad spectrum of human and murine cancers, including BL, CLL, NB, and hepatocellular carcinoma. In addition, our findings indicate that Myc-transformed cancer cells rely on this pathway to sustain cell proliferation and viability. We further identify SCD1 as a critical IRE1α/XBP1 effector required for maintenance of ER homeostasis and prevention of Myc-mediated cytotoxic ER stress.

Disruption of ER-dependent protein folding and transport results in the accumulation of misfolded proteins and consequent activation of ER stress responses. Specifically, cells initiate at least 1 of 3 major UPR-signaling pathways (PERK, IRE1, ATF6) that collectively attenuate protein synthesis, increase protein folding, and elevate protein degradation to sustain cell survival. If these responses do not restore ER homeostasis, persistent UPR signaling can ultimately trigger apoptosis (9). The UPR has recently been appreciated as a central player in tumor development, making it an appealing target in both solid and hematological malignancies (45, 46). However, several fundamental issues need to be addressed to rationally target the UPR and improve patient outcomes. For example, what constitutes cell-autonomous drivers of UPR in different types of cancer and how they function to integrate stress management must be elucidated. In addition, how to identify patients most likely to respond to UPR inhibition remains unclear. In the current study, we determined that both c-Myc and N-Myc overexpression activate the IRE1α/XBP1 pathway through multiple molecular mechanisms. More importantly, this signaling pathway induces SCD1 as a critical downstream effector that generates unsaturated lipids to maintain ER membrane homeostasis in the face of Myc-dependent proteotoxicity. Consistent with our results,

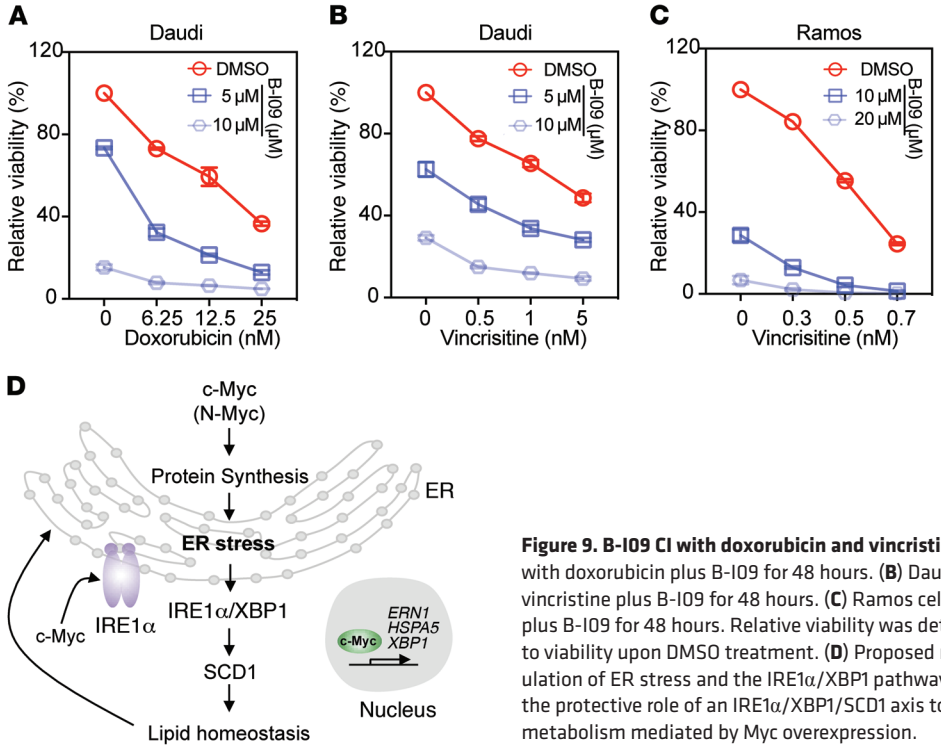


**Figure 9. B-I09 CI with doxorubicin and vincristine.** (**A**) Daudi cells treated with doxorubicin plus B-I09 for 48 hours. (**B**) Daudi cells treated with vincristine plus B-I09 for 48 hours. (**C**) Ramos cells treated with vincristine plus B-I09 for 48 hours. Relative viability was determined by normalizing to viability upon DMSO treatment. (**D**) Proposed model illustrating the regulation of ER stress and the IRE1α/XBP1 pathway by c-Myc and N-Myc and the protective role of an IRE1α/XBP1/SCD1 axis to counterbalance anabolic metabolism mediated by Myc overexpression.

an accompanying report (47) utilizing a triple-negative breast cancer model also demonstrates c-Myc regulation of IRE1α/XBP1 signaling and shows that cells with higher c-Myc expression are more sensitive to pharmacological IRE1α inhibition and genetic XBP1 depletion. Taking these two studies together, we identified IRE1α/XBP1 signaling as a critical survival pathway downstream of Myc activation in multiple cancers; therefore, Myc activation might be utilized to predict responses to IRE1α RNase inhibitor treatment in patients with CLL, NB, and breast cancers.

Previous studies clearly show that XBP1s regulates ER-associated degradation, protein entry into the ER, and protein folding (13, 14). However, to maintain ER homeostasis in cells with oncogene-driven protein synthesis, ER lipid membrane biogenesis must also be regulated to accommodate elevated protein load. For example, our previous studies revealed an essential role for unsaturated lipids in maintaining ER homeostasis and viability in cells with constitutive mTORC1 activity (48). The relationship between the UPR and ER lipid homeostasis is underscored by data demonstrating mutant IRE1α and PERK proteins lacking the ability to sense unfolded proteins retain their responsiveness to increased lipid saturation (49) and showing that SCD1 inhibition initiates ER stress in multiple conditions (50, 51). In this study, we extend the model by demonstrating that IRE1α/XBP1 signaling itself regulates SCD1 expression (Figure 9D). In the case of Myc-transformed cancer cells, this feedback loop is essential for cell proliferation and viability. Interestingly, the accompanying study describes the complex formation of c-Myc/XBP1s in the nucleus; it is possible c-Myc/XBP1s coordinately transcriptionally regulates *SCD*. Carroll et al. found that oncogenic Myc requires the Myc superfamily member MondoA for tumorigenesis (52) and that decreased lipid biosynthesis plays an important role in MondoA-deficient cell death. In our study, we also found that IRE1α RNase inhibition decreased de novo lipogenesis, yet SCD1 loss does not fully explain cellular responses to IRE1α inhibition. Therefore, it is possible that decreased lipid biosynthesis also contributes to the observed phenotypes. Future studies will investigate how Myc, MondoA, and XBP1s coordinate with each other to regulate lipid metabolism. Our results also extend an emerging theme in which oncogenic transformation simultaneously induces anabolic metabolism to increase proliferation along with homeostatic pathways that maintain cell viability. These include lipid and protein scavenging in RAS-transformed tumors (39, 53), autophagy downstream of c-Myc overexpression (10), and lipid storage downstream of HIF2α activation (54).

The role of the IRE1α/XBP1 pathway in human cancers may be more general, as Genovese et al. recently demonstrated that pancreatic ductal adenocarcinoma cells exhibiting a Myc gene-expression signature undergo an anabolic switch that increases protein metabolism and adaptive activation of IRE1α-mediated survival pathways (55). Increased XBP1s levels are frequently associated with human multiple myeloma (56), and disruption of XBP1 splicing by inhibiting IRE1α may be a promising therapeutic option in this and other malignancies. Finally, XBP1s promotes triple-negative breast cancer progression via HIF1α (57), suggesting that different oncogenic pathways may engage distinct downstream UPR responses and therefore harbor nonoverlapping vulnerabilities to specific inhibitors.

Our findings support the use of IRE1α RNase inhibitors as an approach to targeting multiple tumors. BL, characterized by *MYC* translocation and dysregulation, is a highly aggressive malignancy that clinically presents as the most common pediatric cancer in specific geographic locations, such as equatorial Africa, Brazil, and Papua New Guinea. Although intensive chemotherapy can achieve long-term survival, these nontargeted agents are unsafe in older patients due to immune suppression and cannot be efficiently

**Table 1. B-I09 CI with doxorubicin and vincristine in Daudi and Ramos cells.**

| | B-I09 (μM) | CI value |
|---|---|---|
| **B-I09 CI with doxorubicin in Daudi cells** | | |
| **Doxorubicin (nM)** | | |
| 6.25 | 5 | 0.842 |
| 12.5 | 5 | 0.798 |
| 25.0 | 5 | 0.758 |
| 6.25 | 10 | 0.866 |
| 12.5 | 10 | 0.853 |
| 25.0 | 10 | 0.835 |
| **B-I09 CI with vincristine in Daudi cells** | | |
| **Vincristine (nM)** | | |
| 0.5 | 5 | 0.796 |
| 1 | 5 | 0.625 |
| 5 | 5 | 0.700 |
| 0.5 | 10 | 0.659 |
| 1 | 10 | 0.581 |
| 5 | 10 | 0.520 |
| | | |
| **B-I09 CI with Vincristine in Ramos cells** | | |
| **Vincristine (nM)** | **B-I09 (μM)** | **CI value** |
| 0.3 | 10 | 0.995 |
| 0.5 | 10 | 0.785 |
| 0.7 | 10 | 0.618 |
| 0.3 | 20 | 0.797 |
| 0.5 | 20 | 0.547 |
| 0.7 | 20 | 0.437 |

CI was calculated using CompuSyn software. CI of less than 0.9 indicates synergistic effects, CI greater than 0.9 and less than 1.1 indicates additive effects, and CI greater than 1.1 indicates antagonistic effects.

deployed in less developed regions because of the need for extensive supportive care. Thus, targeted treatment strategies with fewer side effects are urgently needed. We provide a proof of principle of combining IRE1α inhibitors with chemotherapy drugs to decrease cytotoxicity and improve survival. In addition, *MYCN* amplification is a major prognostic factor in NB (43); targeting IRE1α underlying N-Myc overexpression is thus a promising strategy for treating a second fatal pediatric disease, where standard of care is extremely difficult and lengthy and imposes substantial toxicities.

## Methods

*Cell culture*. Raji, Daudi, Ramos, EB-2, SK-N-AS, and BE2C cells were obtained from ATCC in 2016, and the Kelly cell line was obtained from Sigma-Aldrich. MEC1, MEC2, and WaC3 cells were described previously (58). The 8498 cells were obtained from Alexander L. Kovalchuk and Herbert C. Morse III (both from the National Institute of Allergy and Infectious Disease, NIH, Rockville, Maryland, USA). N-MycER SHEP cells were described previously (59). Cells were cultured for a maximum of 6 weeks before thawing fresh, early passage cells and routinely confirmed to be *Mycoplasma* negative. Raji, Daudi, Ramos, EB-2, MEC1, MEC2, WaC3, P493, 8498, N-MycER SHEP, and Kelly cells were maintained in RPMI 1640 supplemented with 10% FBS, 2 mM glutamine, and penicillin/streptomycin and cultured in 5% $CO_2$ at 37°C. SK-N-AS cells were cultured in DMEM supplemented with 15% FBS, 2 mM glutamine, 1× nonessential amino acids (NEAA), and penicillin/streptomycin. BE2C cells were maintained in DMEM with 10% FBS, 4 mM glutamine, and penicillin/streptomycin. During experimental conditions, FBS was decreased to 5%, with other components unchanged. For lipid-deprivation experiments, lipid concentration in the culture medium was achieved through the dilution of complete FBS into Delipidized FBS (catalog 900-123, Gemini Bio Products) without changing other components. The P493 cells were derived from human peripheral blood B cells immortalized by an EBV genome that was complemented with an EBV nuclear antigen-estrogen receptor (EBNA2-ER) fusion protein and a tetracycline-repressible c-Myc transgene. With tetracycline (0.1 μg/ml) and β-estradiol (1 μM), which activates EBNA2-ER, the cells proliferated with induction of endogenous c-Myc by EBNA2, achieving a Low Myc state that is equivalent to that of EBV-immortalized B lymphocytes. With tetracycline alone, c-Myc was suppressed and a No Myc state was achieved. In the absence of tetracycline and β-estradiol, ectopic c-Myc was induced in a High Myc tumorigenic state that resembled human BL. In N-MycER SHEP cells, N-MycER activation was performed by treatment with 4-OHT at 200 nM.

*Reagents*. B-I09 was described in a previous publication (23). Tetracycline (catalog 87128), β-estradiol (catalog E8875), CHX (catalog C7698), tunicamycin (catalog T7765), fatty acid–free BSA (catalog A8806), OA (catalog O3008), POA (catalog P9417), sodium palmitate (catalog P9767), 4-OHT (catalog H7904), and doxorubicin hydrochloride (catalog D1515) were purchased from Sigma-Aldrich. JQ1 (catalog 4499) was from TOCRIS, and 4μ8c (catalog 412512) was from Millipore. SCDi (catalog Cay10012562) and vincristine sulfate (catalog 11764) were purchased from Cayman. U-$^{13}$C-glucose (catalog CLM-1396) was from Cambridge Isotope Laboratories.

*Plasmids, virus production and infection*. GIPZ nonsilencing lentiviral shRNA control (clone ID RHS4346) and shRNA-targeting *XBP1* (clone ID V3LHS_387388) were purchased from Dharmacon. Inducible control shRNA (forward: 5′-CCGGCCTAAGGTTAAGTCGCCCTCGCTCGAGCGAGGGCGACTTAACCTTAGGTTTTTG-3′, reverse: 5′-AATTCAAAAACCTAAGGTTAAGTCGCCCTCGCTCGAGCGAGGGCGACTTAACCTTAGG-3′) or *XBP1* shRNA (forward: 5′-CCGGGACCCAGTCATGTTCTTCAAACTCGAGTTTGAAGAACATGACTGGGTCTTTTTG-3′, reverse: 5′-AATTCAAAAAGACCCAGTCATGTTCTTCAAACTCGAGTTTGAAGAACATGACTGGGTC-3′) was cloned in pLKO-Tet-On lentiviral vector. To produce lentiviruses, 293T cells were cotransfected with the lentivirus expression vectors psPAX2 and pMD2.G using FuGENE 6 transfection reagent (catalog E2691, Promega). Lentiviruses were collected 48 hours after transfection. For N-MycER SHEP cells, the infection efficiency was greater than 95% after 2 days infection, examined by GFP-positive cells. For Kelly cells, viruses were used with 8 μg/ml polybrene for infection and cells were selected with 0.75 μg/ml puromycin for 5 days to establish stable cell lines.

*RNA interference*. siRNA pools targeting human *XBP1* (catalog L-009552), *SCD* (catalog L-005061), and nontargeting pool control (catalog D-001810) were from Dharmacon. For P493 cells, $5 \times 10^6$ cells were electroporated using an Amaxa Nucleofector with Program O-06, Nucleofactor Kit V (catalog VCA-1003, Lonza), and 2 μM siRNA for each reaction was used. For N-MycER SHEP cells, lipofectamine RNAiMAX Reagent (catalog 13778, Invitrogen) was employed according to the manufacturer's instructions.

*Viability assays*. Cell viability was determined using the FITC–Annexin V PI Kit (catalog 556547) or APC–Annexin V (catalog 550475) for GFP-positive cells from BD Biosciences according to the manufacturer's instructions. Flow cytometry was performed using the BD Accuri C6 instrument or BD FACSCalibur flow cytometer, and double-negative cells were determined viable.

*Cell growth assay*. BL cell lines and CLL cells were seeded in 6-well plates and exposed to indicated treatments. Cells were counted at various time points using the Invitrogen Countess Automated Cell Counter (catalog C10281) per the manufacturer's instructions. Control SHEP, 4-OHT SHEP, SK-N-AS, BE2C, and Kelly cells were seeded in 96-well plates and exposed to indicated treatments. At indicated time points, cell growth was analyzed using the WTS-1 reagent (catalog 11644807001, Roche) according to the manufacturer's instructions.

*Electron microscopy*. P493 cells with or without c-Myc overexpression were cultured at a concentration of $5 \times 10^5$ cells/ml. Cells were pelleted through centrifugation and washed with PBS once before fixation. After fixation overnight, cells were submitted to the University of Pennsylvania Electron Microscopy Resource Laboratory for analysis. At least 30 cells were analyzed from each group, and representative images are shown.

*RNA extraction, real-time quantitative RT-PCR, and RT-PCR analysis*. Total RNA was isolated using the RNeasy Mini Kit (catalog 74104, QIAGEN), and cDNA was synthesized using the High-Capacity RNA-to-cDNA Kit (catalog 4387406, Thermo Fisher Scientific). Quantitative reverse-transcription PCR (qRT-PCR) was performed on a ViiA7 Real-Time PCR system from Applied Biosystems. Predesigned TaqMan primers were obtained from Thermo Fisher Scientific for the following genes: *TBP* (HS00427620_M1), *ACTB* (HS01060665_G1), *HSPA5* (HS00946084_G1), *MYC* (HS00153408_M1), *MYCN* (HS00232074_M1), *XBP1t* (HS00231936_M1), *XBP1s* (HS03929085_G1), *LDHA* (HS01378790_G1), *ERN1* (HS00176385_M1), *LXR* (HS00172885_M1), *FABP5* (HS02339437_G1), *PPARA* (HS00947536_M1), *ACACA* (HS01046047_M1), *ACACB* (Hs01565914_m1), *FABP6* (HS01031183_M1), *PPARD* (HS04187066_G1), *ACAT1* (HS00608002_M1), *CPT1A* (HS00912671_M1), *CPT1B* (HS03046298_S1), *SCD* (HS01682761_M1), *ACLY* (HS00982738_M1), *FASN* (HS01005622_M1), *ACSS2* (HS01122829_M1), *DGAT1* (HS01017541_M1), *DGAT2* (HS01045913_M1), *PLIN2* (HS00605340_M1), *PLIN3* (HS00998416_M1), *HMGCS1* (HS00940429_M1), *HMGCR* (HS00168352_M1), *ODC1* (HS00159739_M1), *HERPUD1* (HS01124269_M1), *DNAJB9* (HS01052402_M1), *ATF3* (HS00231069_M1), and *DDIT3* (HS00358796_G1). VeriQuest Fast Probe qPCR Master Mix (catalog 75680) was purchased from Affymetrix. SYBR Green primers were utilized for mouse *Actb* (forward: 5′-AAATCTGGCACCACACCTTC-3′, reverse: 5′-GGGGTGTTGAAGGTCTCAAA-3′), mouse *Xbp1t* (forward: 5′-GGCTGTCTGGCCTTAGAAGA-3′, reverse: 5′-CTGTCAAATGACCCTCCCTG-3′), mouse *Xbp1s* (forward: 5′-GAGTCCGCAGCAGGTG-3′, reverse: 5′-GTGTCAGAGTCCATGGGA-3′), human *XBP1t* (forward: 5′-GGCATCCTGGCTTGCCTCCA-3′, reverse: 5′-GCCCCCTCAGCAGGTGTTCC-3′), and human *XBP1s* (forward: 5′-CTGAGTCCGCAGCAGGTG-3′, reverse: 5′-TCCAAGTTGTCCAGAATGCC-3′). SYBR Green PCR Master Mix was purchased from Thermo Fisher Scientific (catalog 4309155). RT-PCR assay for *XBP1* splicing was described previously (24). Primers for *XBP1* were as follows: forward: 5′-CCTGGTTGCTGAAGAGGAGG-3′, reverse: 5′-CCATGGGGAGATGTTCTGGAG-3′. Primers for internal control *18S rRNA* were as follows: forward: 5′-GGCCCTGTAATTGGAATGAGTC-3′, reverse: 5′-CCAAGATCCAACTACGAGCTT-3′.

*Western blot analysis*. Cells were lysed in 150 mM NaCl, 10 mM Tris pH 7.6, 0.1% SDS, and 5 mM EDTA containing Roche cOmplete ULTRA Protease/Phosphatase Inhibitor (catalog 05892791001). Nuclear fractionation was performed using NE-PER Nuclear and Cytoplasmic Extraction Reagents (catalog 78833, Thermo Fisher Scientific). Protein concentration was quantified with Pierce BCA Protein Assay Kit (catalog 23225, Thermo Fisher Scientific). Isolated proteins were resolved by SDS-PAGE, and Western blot analysis was performed. IRE1α phosphorylation was monitored by Phos-tag SDS-PAGE (Wako Pure Chemical Industries Ltd.) as described previously (60). All primary antibodies were diluted in 1:1,000 in 5% w/v nonfat milk, unless otherwise noted. Blots were incubated with primary antibodies overnight at 4°C. XBP1s (catalog 619502, 1:500) antibody was from BioLegend. c-Myc (catalog ab32072), actin (catalog ab3280), and SCD1 (catalog ab19862) antibodies were purchased from Abcam. IRE1α (catalog 3294), BiP (catalog 3177), PARP (catalog 9542), GAPDH (catalog 2118), total JNK (catalog 9252), phospho-threonine 183/185 JNK (catalog 9251), p62 (catalog 5114), LC3B (catalog 2775), N-Myc (catalog 9405), and HDAC1 (catalog 5356) antibodies were purchased from Cell Signaling Technology. DDRGK1 antibody (catalog HPA013373) was from Sigma-Aldrich. HRD1 antibody (catalog NB100-2526) was from Novus. SEL1L antibody was generated in our laboratory. Primary antibodies were detected using horseradish peroxidase–conjugated secondary antibodies (Cell Signaling Technology) followed by exposure to enhanced chemiluminescence substrate (catalog NEL103001EA, PerkinElmer) or SuperSignal West Femto Maximum Sensitivity Substrate (catalog 34095, Thermo Fisher Scientific).

*ChIP and ChIP-qPCR assay*. This assay was performed as described previously (57). qPCR using SYBR Green was performed per the manufacturer's protocol. The primers used for positive control ERdj4 were as follows: forward: 5′-GCAGCAACAACAGTTTTCCA-3′, reverse: 5′-GCACCCTAATCTCGGTCGTA-3′. Primers for negative control were as follows: forward: 5′-TTCAGGGGAAGAAAAACTTGGGA-3′ and reverse: 5′-TCCGAAAAACCCCTGCACTC-3′, which is located upstream of the *SCD* promoter. Primers for XBP1s binding site within the *SCD* promoter region were as follows: forward: 5′-AGAGGGAACAGCAGATTGCG-3′, reverse: 5′-CTGTAAACTCCGGCTCGTCA-3′.

*Analysis of lipids by fatty acid methyl esterification*. Gas chromatography/MS (GC/MS) analysis was used to examine total cellular fatty acids either with or without $^{13}C$ enrichment. U-$^{13}C$-glucose was used to allow differentiation between de novo– and non de novo–produced lipids. For $^{13}C$ enrichment studies, cells were cultured in RPMI 1640 medium (catalog 11879020, Thermo Fisher Scientific) and supplemented with 5% dialyzed FBS (catalog 100-108, Gemini Bio Products), with all unenriched glucose replaced with U-$^{13}C$-glucose. Cells were cultured to a level of $5 \times 10^5$/ml in T-75 flasks. Subsequently, they were collected by centrifugation and washed 3 times with ice-cold PBS. The second PBS wash contained 1% fatty acid–free albumin to remove residual lipids from the medium. After the last centrifugation, 1 ml of cold methanol was added prior to storage at –80°C. A standard Bligh-Dyer chloroform extraction was used to recover both polar and nonpolar lipids (61). Cells were initially sonicated in 2.7 ml of 75% methanol/25% water. Subsequently, chloroform and water were added, resulting in a final mixture containing 38:31:31 of methanol/water/chloroform. The mixture separated into 2 phases with the lipids in a

chloroform-rich hydrophobic phase. After centrifugation, the bottom hydrophobic phase (~1.3 ml) was removed with a glass pipette. A second extraction with 0.7 ml chloroform was used to recover additional lipids from the methanol/water phase. The 2 hydrophobic fractions were combined in a single glass centrifuge tube and back extracted with 0.15 ml of deionized water. The hydrophobic fraction was dried under nitrogen in 30-ml thick-wall glass anaerobic tubes.

The dried lipid extracts were dissolved in 2 ml of a 4:1 methanol/toluene mixture that contained butylated hydroxytoluene (0.45 mM). Acetylchloride (14 mM) was added to produce catalytic $H^+$ in situ for the methyl esterification reaction. The anaerobic tubes containing the reaction mixtures were capped with thick butyl rubber stoppers (Bellco) and heated at 100°C for 1 hour. After cooling, the reaction mixtures were mixed with 0.56 M aqueous sodium carbonate at a ratio of 2:5 to drive the fatty acid methyl esters into a hydrophobic phase that floated on top of the aqueous phase. The toluene was purified by centrifugation and analyzed with an Agilent 7890A GC/MS (7890A/5975C). Mass spectra were quantified with MSD ChemStation software from Agilent. Isocor, written for the Python programming environment (www.python.org), was used to correct mass spectra for natural abundance contributions from $^{13}C$. Mean enrichment was calculated as follows:

$$Mean\_enrichment = \frac{\sum_{i=1}^{n} f_i \times i}{n}$$

(Equation 1)

where $f_i$ = fractional enrichment of the $i$-th carbon and $n$ is the total number of carbons.

*Cell staining and imaging*. P493 cells were cytospun onto the slides through the CytoSep Dual Sample Chamber (catalog M967-20FW, Medline Industries Inc.) in a 7620 Cytopro Cytocentrifuge (Wescor) at 212 *g* for 7 minutes. For immunofluorescence, slides were incubated with 50 mM ammonium chloride for 10 minutes, permeabilized with 0.25% Triton X-100 for 10 minutes, and blocked with 2% BSA for 30 minutes. Slides were then incubated with Ki-67 primary antibody (catalog 550609, BD Biosciences — Pharmingen) at 1:100. Secondary Alex Fluor 594 goat anti-mouse antibody (catalog R37121, Thermo Fisher Scientific) was used at 1:200 for 1 hour at room temperature. Slides were mounted in ProLong Gold Antifade with DAPI (catalog P36935, Thermo Fisher Scientific) before imaging. TUNEL staining was performed using ApopTag Plus Fluorescein In Situ Apoptosis Detection Kit (catalog S7111, Millipore) according to the manufacturer's instructions.

*OA, Palm, and POA treatment*. OA-BSA conjugation solution was purchased from Sigma Aldrich. In this solution, OA was dissolved in 10% BSA; the concentration of OA is 3.33 mM. For Palm and POA, the powder was dissolved in 50% ethanol at 65°C to achieve a 50 mM stock and then conjugated with BSA in a 10% BSA solution to a concentration of 3.33 mM at 37°C for 1 hour. For the combination treatment, OA and Palm were added 1:1 to the medium.

*Xenograft tumors*. For P493 High Myc xenografts and B-I09 treatment, $1.5 \times 10^7$ P493 High Myc cells were injected subcutaneously into the flanks of 6-week-old female homozygous athymic nude mice (strain code 490, Charles River Laboratories). When the tumor volumes reached approximately 150 $mm^3$, B-I09 was administered intraperitoneally at 50 mg/kg on the first 5 days of each week for 2 weeks. For Ramos xenografts and SCDi treatment, $1 \times 10^6$ Ramos cells were introduced subcutaneously into the flanks of 10-week-old female homozygous C.B-17 SCID mice (strain code 236, Charles River Laboratories). When tumor volumes reached approximately 50–50 $mm^3$, SCDi was orally administered at 5 mg/kg (dissolved in 0.5% methyl cellulose) twice daily. For Kelly xenografts, $3 \times 10^6$ Kelly cells with tet-inducible SCR or tet-inducible shXBP1 construct were injected subcutaneously into the left or right flanks of 5-week-old homozygous female BALB/c nude mice (strain code 194, Charles River Laboratories), respectively. When the tumor volumes reached approximately 50–150 $mm^3$, dox diet (catalog S3888, Bio-Serv) was administered to the mice. Tumor volume was monitored by caliper measurements.

*Mice, tumor formation, and B cell purification*. Mice carrying the human *MYC* oncogene under the control of the Igλ regulatory elements (62) were crossed with WT C57BL/6J mice (mouse strain 000664, The Jackson Laboratory), monitored for lymphoma development, and sacrificed when moribund (3 to 5 months old). Total RNA from superficial cervical lymphomas and mesenteric lymphomas from the same mouse was extracted for further analysis. For WT B cell purification, naive B lymphocytes were purified from C57BL/6J mouse spleens by magnetic depletion of CD43-positive cells (Miltenyi Biotech) according to the manufacturer's instructions. *LAP/MYC* mice were described previously (63). mRNA was extracted from 5 liver tumors and paired normal liver tissues from this mouse model for qRT-PCR analysis.

*Statistics*. In Supplemental Figure 5I and Supplemental 6, C and D, the contribution ratios of BSA were calculated using relative viability of B-I09+BSA to divide B-I09 treatment alone, while the contribution ratios of OA were calculated using relative viability of B-I09+OA to divide B-I09+BSA. For the correlation between *HSPA5* expression and Myc signature (Supplemental Figure 1A, and Supplemental Table 1), raw data for 22 samples of interest in GSE2350 were downloaded from NCBI's Gene Expression Omnibus (GEO) database. Robust multi-array average (RMA) was performed separately on the 9 and 13 samples, which were run on HG_U95A and HG_U95Av2, respectively. Resulting $\log_2$-transformed normalized intensities were quantile normalized across all samples to lessen the platform-specific effects. Correlation of all genes across all samples was calculated against *HSPA5* (probeset ID 36614_at). *P* values and false discovery rate–corrected (FDR-corrected) *P* values were calculated for each gene. The set of genes with corrected *P* values of less than or equal to 0.01 (106 genes) was overlapped with the set of genes described to be Myc-related in the Hallmark sets from MSigDB (Myc Union, 240 genes). A Fisher's exact test was performed showing the overlap between these 2 lists and the full set of genes included in the array design. Six genes from the 2 lists significantly overlapped ($P = 0.0364$). Where necessary, data were statistically analyzed to generate mean ± SD. The levels of significance were determined using 2-tailed Student's *t* test, 2-way ANOVA with Bonferroni's correction, or 2-tailed paired *t* test. Where appropriate, *P* values are provided in the figures or in the legends. $P < 0.05$ was considered statistically significant.

*Study approval*. All experiments involving the use of mice were performed following protocols approved by the Institutional Animal Care and Use Committee at the University of Pennsylvania.

## Author contributions

HX and MCS designed all research studies. HX, CHAT, JHS, AM, JC, RL, and DJS conducted experiments and acquired data. JRDV, YX,

CVD, and CCAH provided reagents. HX, CHAT, JHS, BK, CCAH, and MCS analyzed data. HX, BK, and MCS wrote the manuscript.

## Acknowledgments

The authors thank Michael L. Atchison (University of Pennsylvania) for providing *Eλ/MYC* mice and Herbert C. Morse III and Alexander L. Kovalchuk (both from the National Institute of Allergy and Infectious Diseases, NIH, Rockville, Maryland, USA) for the 8498 cell line. This work was supported by National Cancer Institute (NCI) grant CA104838 (to MCS), NCI grant CA163910 (to CCAH), NCI grant CA190860 (to CCAH and JRDV), NCI grant CA199553 (to JRDV), and an Alex's Lemonade Stand Foundation Fellowship (to HX).

Address correspondence to: M. Celeste Simon, Abramson Family Cancer Research Institute, 456 BRB II/III, 421 Curie Boulevard, Philadelphia, Pennsylvania 19104, USA. Phone: 215.746.5532; Email: celeste2@mail.med.upenn.edu.

1. Dang CV. MYC on the path to cancer. *Cell*. 2012;149(1):22–35.
2. Malynn BA, et al. N-myc can functionally replace c-myc in murine development, cellular growth, and differentiation. *Genes Dev*. 2000;14(11):1390–1399.
3. Gabay M, Li Y, Felsher DW. MYC activation is a hallmark of cancer initiation and maintenance. *Cold Spring Harb Perspect Med*. 2014;4(6):a014241.
4. Kiessling A, Wiesinger R, Sperl B, Berg T. Selective inhibition of c-Myc/Max dimerization by a pyrazolo[1,5-a]pyrimidine. *ChemMedChem*. 2007;2(5):627–630.
5. Delmore JE, et al. BET bromodomain inhibition as a therapeutic strategy to target c-Myc. *Cell*. 2011;146(6):904–917.
6. Puissant A, et al. Targeting MYCN in neuroblastoma by BET bromodomain inhibition. *Cancer Discov*. 2013;3(3):308–323.
7. McKeown MR, Bradner JE. Therapeutic strategies to inhibit MYC. *Cold Spring Harb Perspect Med*. 2014;4(10):a014266.
8. Barna M, et al. Suppression of Myc oncogenic activity by ribosomal protein haploinsufficiency. *Nature*. 2008;456(7224):971–975.
9. Hetz C. The unfolded protein response: controlling cell fate decisions under ER stress and beyond. *Nat Rev Mol Cell Biol*. 2012;13(2):89–102.
10. Hart LS, et al. ER stress-mediated autophagy promotes Myc-dependent transformation and tumor growth. *J Clin Invest*. 2012;122(12):4621–4634.
11. Nagy P, Varga A, Pircs K, Hegedűs K, Juhász G. Myc-driven overgrowth requires unfolded protein response-mediated induction of autophagy and antioxidant responses in Drosophila melanogaster. *PLoS Genet*. 2013;9(8):e1003664.
12. Chen Y, Brandizzi F. IRE1: ER stress sensor and cell fate executor. *Trends Cell Biol*. 2013;23(11):547–555.
13. Lee AH, Iwakoshi NN, Glimcher LH. XBP-1 regulates a subset of endoplasmic reticulum resident chaperone genes in the unfolded protein response. *Mol Cell Biol*. 2003;23(21):7448–7459.
14. Acosta-Alvear D, et al. XBP1 controls diverse cell type- and condition-specific transcriptional regulatory networks. *Mol Cell*. 2007;27(1):53–66.
15. Hollien J, Lin JH, Li H, Stevens N, Walter P, Weissman JS. Regulated Ire1-dependent decay of messenger RNAs in mammalian cells. *J Cell Biol*. 2009;186(3):323–331.
16. Schmitz R, Ceribelli M, Pittaluga S, Wright G, Staudt LM. Oncogenic mechanisms in Burkitt lymphoma. *Cold Spring Harb Perspect Med*. 2014;4(2):a014282.
17. Basso K, Margolin AA, Stolovitzky G, Klein U, Dalla-Favera R, Califano A. Reverse engineering of regulatory networks in human B cells. *Nat Genet*. 2005;37(4):382–390.
18. Brune V, et al. Origin and pathogenesis of nodular lymphocyte-predominant Hodgkin lymphoma as revealed by global gene expression analysis. *J Exp Med*. 2008;205(10):2251–2268.
19. So JS, et al. Silencing of lipid metabolism genes through IRE1α-mediated mRNA decay lowers plasma lipids in mice. *Cell Metab*. 2012;16(4):487–499.
20. Yustein JT, et al. Induction of ectopic Myc target gene JAG2 augments hypoxic growth and tumorigenesis in a human B-cell model. *Proc Natl Acad Sci U S A*. 2010;107(8):3534–3539.
21. Liu J, et al. A critical role of DDRGK1 in endoplasmic reticulum homoeostasis via regulation of IRE1α stability. *Nat Commun*. 2017;8:14186.
22. Sun S, et al. IRE1α is an endogenous substrate of endoplasmic-reticulum-associated degradation. *Nat Cell Biol*. 2015;17(12):1546–1555.
23. Tang CH, et al. Inhibition of ER stress-associated IRE-1/XBP-1 pathway reduces leukemic cell survival. *J Clin Invest*. 2014;124(6):2585–2598.
24. Oslowski CM, Urano F. Measuring ER stress and the unfolded protein response using mammalian tissue culture system. *Meth Enzymol*. 2011;490:71–92.
25. Cross BC, et al. The molecular basis for selective inhibition of unconventional mRNA splicing by an IRE1-binding small molecule. *Proc Natl Acad Sci U S A*. 2012;109(15):E869–E878.
26. Lee AH, Scapa EF, Cohen DE, Glimcher LH. Regulation of hepatic lipogenesis by the transcription factor XBP1. *Science*. 2008;320(5882):1492–1496.
27. Molyneux EM, et al. Burkitt's lymphoma. *Lancet*. 2012;379(9822):1234–1244.
28. Urano F, et al. Coupling of stress in the ER to activation of JNK protein kinases by transmembrane protein kinase IRE1. *Science*. 2000;287(5453):664–666.
29. Margariti A, et al. XBP1 mRNA splicing triggers an autophagic response in endothelial cells through BECLIN-1 transcriptional activation. *J Biol Chem*. 2013;288(2):859–872.
30. Tian PG, Jiang ZX, Li JH, Zhou Z, Zhang QH. Spliced XBP1 promotes macrophage survival and autophagy by interacting with Beclin-1. *Biochem Biophys Res Commun*. 2015;463(4):518–523.
31. Piperi C, Adamopoulos C, Papavassiliou AG. XBP1: a pivotal transcriptional regulator of glucose and lipid metabolism. *Trends Endocrinol Metab*. 2016;27(3):119–122.
32. Cubillos-Ruiz JR, et al. ER stress sensor XBP1 controls anti-tumor immunity by disrupting dendritic cell homeostasis. *Cell*. 2015;161(7):1527–1538.
33. McGehee AM, et al. XBP-1-deficient plasmablasts show normal protein folding but altered glycosylation and lipid synthesis. *J Immunol*. 2009;183(6):3690–3699.
34. Kamphorst JJ, Fan J, Lu W, White E, Rabinowitz JD. Liquid chromatography-high resolution mass spectrometry analysis of fatty acid metabolism. *Anal Chem*. 2011;83(23):9114–9122.
35. Eberlin LS, et al. Alteration of the lipid profile in lymphomas induced by MYC overexpression. *Proc Natl Acad Sci U S A*. 2014;111(29):10450–10455.
36. Kamphorst JJ, et al. Hypoxic and Ras-transformed cells support growth by scavenging unsaturated fatty acids from lysophospholipids. *Proc Natl Acad Sci U S A*. 2013;110(22):8882–8887.
37. Young RM, et al. Dysregulated mTORC1 renders cells critically dependent on desaturated lipids for survival under tumor-like stress. *Genes Dev*. 2013;27(10):1115–1131.
38. Zeller KI, Jegga AG, Aronow BJ, O'Donnell KA, Dang CV. An integrated database of genes responsive to the Myc oncogenic transcription factor: identification of direct genomic targets. *Genome Biol*. 2003;4(10):R69.
39. Commisso C, et al. Macropinocytosis of protein is an amino acid supply route in Ras-transformed cells. *Nature*. 2013;497(7451):633–637.
40. Palm W, Park Y, Wright K, Pavlova NN, Tuveson DA, Thompson CB. The utilization of extracellular proteins as nutrients is suppressed by mTORC1. *Cell*. 2015;162(2):259–270.
41. Francis GL. Albumin and mammalian cell culture: implications for biotechnology applications. *Cytotechnology*. 2010;62(1):1–16.
42. Mason P, et al. SCD1 inhibition causes cancer cell death by depleting mono-unsaturated fatty acids. *PLoS ONE*. 2012;7(3):e33823.
43. Huang M, Weiss WA. Neuroblastoma and MYCN. *Cold Spring Harb Perspect Med*. 2013;3(10):a014415.
44. Hoffman B, Liebermann DA. Apoptotic signaling by c-MYC. *Oncogene*. 2008;27(50):6462–6472.
45. Clarke HJ, Chambers JE, Liniker E, Marciniak SJ. Endoplasmic reticulum stress in malignancy. *Cancer Cell*. 2014;25(5):563–573.
46. Urra H, Dufey E, Avril T, Chevet E, Hetz C. Endoplasmic reticulum stress and the hallmarks of cancer. *Trends Cancer*. 2016;2(5):252–262.
47. Zhao N, et al. Pharmacological targeting of MYC-regulated IRE1/XBP1 pathway suppresses

MYC-driven breast cancer. *J Clin Invest*. https://doi.org/10.1172/JCI95873.
48. Young RM, et al. Dysregulated mTORC1 renders cells critically dependent on desaturated lipids for survival under tumor-like stress. *Genes Dev*. 2013;27(10):1115–1131.
49. Volmer R, van der Ploeg K, Ron D. Membrane lipid saturation activates endoplasmic reticulum unfolded protein response transducers through their transmembrane domains. *Proc Natl Acad Sci U S A*. 2013;110(12):4628–4633.
50. von Roemeling CA, et al. Stearoyl-CoA desaturase 1 is a novel molecular therapeutic target for clear cell renal cell carcinoma. *Clin Cancer Res*. 2013;19(9):2368–2380.
51. Liu X, Strable MS, Ntambi JM. Stearoyl CoA desaturase 1: role in cellular inflammation and stress. *Adv Nutr*. 2011;2(1):15–22.
52. Carroll PA, et al. Deregulated Myc requires MondoA/Mlx for metabolic reprogramming and tumorigenesis. *Cancer Cell*. 2015;27(2):271–285.
53. Kamphorst JJ, et al. Hypoxic and Ras-transformed cells support growth by scavenging unsaturated fatty acids from lysophospholipids. *Proc Natl Acad Sci U S A*. 2013;110(22):8882–8887.
54. Qiu B, et al. HIF2α-dependent lipid storage promotes endoplasmic reticulum homeostasis in clear-cell renal cell carcinoma. *Cancer Discov*. 2015;5(6):652–667.
55. Genovese G, et al. Synthetic vulnerabilities of mesenchymal subpopulations in pancreatic cancer. *Nature*. 2017;542(7641):362–366.
56. Mimura N, et al. Blockade of XBP1 splicing by inhibition of IRE1α is a promising therapeutic option in multiple myeloma. *Blood*. 2012;119(24):5772–5781.
57. Chen X, et al. XBP1 promotes triple-negative breast cancer by controlling the HIF1α pathway. *Nature*. 2014;508(7494):103–107.
58. Kriss CL, et al. Overexpression of TCL1 activates the endoplasmic reticulum stress response: a novel mechanism of leukemic progression in mice. *Blood*. 2012;120(5):1027–1038.
59. Ushmorov A, Hogarty MD, Liu X, Knauss H, Debatin KM, Beltinger C. N-myc augments death and attenuates protective effects of Bcl-2 in trophically stressed neuroblastoma cells. *Oncogene*. 2008;27(24):3424–3434.
60. Yang L, Xue Z, He Y, Sun S, Chen H, Qi L. A Phos-tag-based approach reveals the extent of physiological endoplasmic reticulum stress. *PLoS One*. 2010;5(7):e11621.
61. Bligh EG, Dyer WJ. A rapid method of total lipid extraction and purification. *Can J Biochem Physiol*. 1959;37(8):911–917.
62. Kovalchuk AL, et al. Burkitt lymphoma in the mouse. *J Exp Med*. 2000;192(8):1183–1190.
63. Xiang Y, et al. Targeted inhibition of tumor-specific glutaminase diminishes cell-autonomous tumorigenesis. *J Clin Invest*. 2015;125(6):2293–2306.